Journal of Computational Physics 245 (2013) 84–106

Contents lists available at SciVerse ScienceDirect

Journal of Computational Physics

journal homepage: www.elsevier.com/locate/jcp

Generalized image charge solvation model for electrostatic interactions in molecular dynamics simulations of aqueous solutions

Shaozhong Deng [a,*], Changfeng Xue [b,*], Andriy Baumketner [c], Donald Jacobs [c], Wei Cai [a]

[a] Department of Mathematics and Statistics, University of North Carolina at Charlotte, Charlotte, NC 28223, United States
[b] Department of Fundamental Sciences, Yancheng Institute of Technology, Yancheng, Jiangsu 224051, PR China
[c] Department of Physics and Optical Science, University of North Carolina at Charlotte, Charlotte, NC 28223, United States

ARTICLE INFO

Article history:
Received 6 June 2012
Received in revised form 6 March 2013
Accepted 12 March 2013
Available online 27 March 2013

Keywords:
Method of images
Reaction field
Electrostatic interaction
Hybrid explicit/implicit solvation model

ABSTRACT

This paper extends the image charge solvation model (ICSM) [Y. Lin, A. Baumketner, S. Deng, Z. Xu, D. Jacobs, W. Cai, An image-based reaction field method for electrostatic interactions in molecular dynamics simulations of aqueous solutions, J. Chem. Phys. 131 (2009) 154103], a hybrid explicit/implicit method to treat electrostatic interactions in computer simulations of biomolecules formulated for spherical cavities, to prolate spheroidal and triaxial ellipsoidal cavities, designed to better accommodate non-spherical solutes in molecular dynamics (MD) simulations. In addition to the utilization of a general truncated octahedron as the MD simulation box, central to the proposed extension is an image approximation method to compute the reaction field for a point charge placed inside such a non-spherical cavity by using a single image charge located outside the cavity. The resulting generalized image charge solvation model (GICSM) is tested in simulations of liquid water, and the results are analyzed in comparison with those obtained from the ICSM simulations as a reference. We find that, for improved computational efficiency due to smaller simulation cells and consequently a less number of explicit solvent molecules, the generalized model can still faithfully reproduce known static and dynamic properties of liquid water at least for systems considered in the present paper, indicating its great potential to become an accurate but more efficient alternative to the ICSM when bio-macromolecules of irregular shapes are to be simulated.

1. Introduction

Electrostatic interactions are well known to play an essential role in the structure, dynamics, and function of biological macromolecules; as such, fast and accurate evaluation of electrostatic interactions in molecular systems remains a major research topic in computer simulations of biomolecules. Electrostatic interactions are long-range, and strongly dependent on the solvent surrounding the biomolecule under study. When modeling biological systems numerically, however, it has been one of the most challenging tasks to account for such solvent environment in a manner that is not only computationally efficient but also physically accurate at the same time. Over the past several decades, various solvation models have been introduced to treat electrostatic interactions in biomolecules the overwhelming majority of which, however, can be broadly divided into explicit [1–3], implicit [4,5], and hybrid explicit/implicit categories [6–8], respectively.

* Corresponding authors. Tel.: +1 704 687 6657; fax: +1 704 687 6415 (S. Deng).
E-mail addresses: shaodeng@uncc.edu (S. Deng), chfxue@gmail.com (C. Xue).

0021-9991/$ - see front matter © 2013 Elsevier Inc. All rights reserved.
http://dx.doi.org/10.1016/j.jcp.2013.03.027

Probably still being the most widely-used approach, explicit solvation models adopt a full-atom representation of both the macromolecule and the surrounding solvent, and thus can offer a detailed and accurate description of the biological system under study; see Fig. 1(a). But all-atom simulations are expensive to perform due to the large number of particles associated with the solvent; as a result, large explicitly solvated systems typically cannot be simulated for biologically relevant timescales. Alternatively, implicit solvation models treat the macromolecule still in atomic detail but the entire solvent surrounding the macromolecule is modeled as a dielectric continuum typically with a large dielectric constant (60–85), while the volume occupied by the macromolecule is modeled as a dissimilar dielectric continuum typically with a low dielectric constant (1–4); see Fig. 1(b). The neglect of explicit solvent molecules can significantly improve the computational efficiency, but on the other hand, the physical accuracy could be greatly decreased since the important atomic details of how the solvent molecules interact with the surface of the macromolecule are ignored. Finally, as a promising method designed to combine good elements of both explicit and implicit approaches, hybrid solvation models represent the macromolecule together with solvent molecules adjacent to the surface of the macromolecule in atomic detail but treat the remaining solvent implicitly as a dielectric continuum; see Fig. 1(c). Since they can not only benefit the efficiency of implicit solvents for replacing the solvent that gives rise to much of the computational cost by a dielectric continuum but also directly model structural effects of the solvent in the proximity of the macromolecule, the hybrid solvation models have received much recent attention.

The present paper concerns fast and accurate computation of electrostatic interactions in hybrid explicit/implicit solvent biomolecular dynamics simulations. While they could differ greatly in their complexity and technical details, as pointed out in Ref. [9], all hybrid solvation models share a common design framework: the central part of a simulated system contains the explicit solute as well as some explicit solvent while the remaining part is treated as a dielectric continuum, as shown in Fig. 1(c). Moreover, to reduce the surface artifacts such as the well-known divergence of the so-called self-polarization potential in the proximity of the abrupt dielectric interface between these two parts, they could also be separated by a buffer layer in which solvent molecules are treated atomically but experience forces different from those present in the central part. There are two types of electrostatic potentials that apply to the charges in the explicit solvent/solute region. One, denoted by Φ_S, is the direct Coulomb potential through which they interact with each another. And the other one, referred to as reaction field and denoted by Φ_{RF}, is an indirect potential that results from the polarization of the continuum solvent region by the explicit charges. The total potential inside the explicit solvent/solute region is thus expressed as $\Phi = \Phi_S + \Phi_{RF}$. Although numerous hybrid electrostatic solvation models have been developed with complementary strengths and weaknesses, the major difference among them lies in the way how Φ_{RF} is computed. The readers are referred to Ref. [9] for a brief survey of some existing hybrid models, including their specific advantages and drawbacks.

In Ref. [9], a new hybrid solvation model, termed the image charge solvation model (ICSM) [10], was proposed for simulations of biomolecules in aqueous solutions. In this model, the central part of the simulated system containing the solute and some solvent is considered in atomic detail, and for computational efficiency, a *regular* truncated octahedron is used for the molecular dynamics (MD) simulation box. Around the simulation box is a *spherical* buffer layer of low thickness where periodic boundary conditions (PBCs) are employed for non-electrostatic interactions to minimize surface effects; see Fig. 4. The solvent outside the buffer layer is then modeled as a dielectric continuum, thus avoiding unphysical interactions between periodic images of the solute commonly used in the lattice-sum explicit solvent simulations. The effect of the dielectric continuum on the solute is treated through reaction field corrections which are calculated approximately by the Friedman image method [11], or for improved computational accuracy, by a more general multiple-image charge method [12]. As a consequence of the image approximation of the reaction field corrections, this model can be combined straightforwardly with fast multipole methods (FMMs) [13,14], giving us an asymptotically optimal $O(N)$ hybrid solvation model for computation of electrostatic interactions in biomolecular systems.

The present paper intends to explore the feasibility of extending the hybrid ICSM formulated for spherical cavities to more general cavities so as to simulate non-spherical solutes more efficiently. More specifically, instead of using a regular

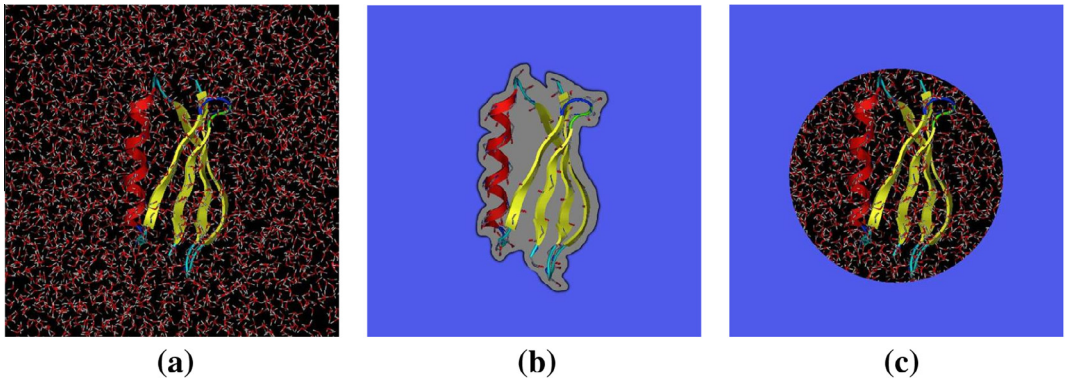

Fig. 1. Three solvation models for electrostatic interactions in computer simulations of biomolecules: (a) explicit, (b) implicit, and (c) hybrid explicit/implicit.

truncated octahedron as the MD simulation box and correspondingly a spherical cavity for the explicit solvent/solute, we utilize a general truncated octahedron simulation box and correspondingly a prolate spheroidal, or more generally a triaxial ellipsoidal cavity. Accordingly, the resulting model is termed the generalized image charge solvation model (GICSM). It should be mentioned that such an extension may be desirable since, for non-spherical bio-macromolecules such as certain globular proteins and other elongated biopolymers like actin and DNA, from the computational point of view using a regular MD simulation box and a spherical cavity to accommodate them may be inefficient, and rather, it may be more beneficial to adopt spheroidal or ellipsoidal cavities for the explicit solvent/solute that can conform more closely to the irregular shapes of the biomolecules under study than a spherical cavity does.

The paper is organized as follows. In Section 2, the ICSM using the regular truncated octahedron as the simulation box and a spherical cavity for the explicit solvent/solute is briefly reviewed. In Section 3, we introduce the GICSM by considering a general truncated octahedron as the simulation box and a prolate spheroidal or triaxial ellipsoidal cavity for the explicit solvent/solute. In particular, we focus on how Φ_{RF} is computed in the generalized model by the method of images. Next in Section 4, some implementation details pertinent to the use of the general truncated octahedron simulation box are discussed, including how to locate periodic images in the buffer layer, how to bookkeep the simulated system when explicit particles cross the boundary of the simulation box, and how to calculate short-range, non-electrostatic interactions. Then for validating the GICSM, in Section 5 it is applied to study liquid water and like in Ref. [9], several structural and dynamic properties of the simulated water are investigated in comparison with those obtained from the ICSM simulations. It is concluded that the GICSM using the same optimal model parameters as those obtained for the original ICSM can also faithfully produce known static and dynamic properties of the simulated liquid water, at least when spheroidal simulation boxes of relatively small aspect ratios are used. Finally, our conclusions and outlook are presented in Section 6. In addition, an image approximation of the reaction field inside a perfectly conducting prolate spheroid influenced by an external point charge is given in Appendix.

2. The hybrid image charge solvation model

For the sake of completeness, the image charge solvation model (ICSM), whose details can be found in a previous paper [9], is briefly outlined here.

2.1. Method of images for calculating reaction field in spherical cavities

As indicated earlier, the hybrid ICSM is a reaction field-based approach formulated for simulations of bio-macromolecules of spherical shape, and how to compute the reaction field inside a spherical cavity is the key theoretical and algorithmic component of the model. To this end, let us consider a spherical dielectric volume V_{in} of radius a and dielectric permittivity ϵ_i embedded in an infinite solvent bath V_{out} of dielectric permittivity ϵ_o, as shown in Fig. 2. Assume that the spherical cavity V_{in} contains a total of N explicit charges of the solute and solvent molecules, say $q_i,\ i = 1, 2, \ldots, N$, located respectively at $\mathbf{r}_i,\ i = 1, 2, \ldots, N$. Then, mathematically, it is well known that the total electrostatic potential $\Phi_{in}(\mathbf{r})$ inside the cavity V_{in} satisfies the following Poisson equation:

$$\epsilon_i \Delta \Phi_{in}(\mathbf{r}) = -\rho_{in}(\mathbf{r}), \tag{1}$$

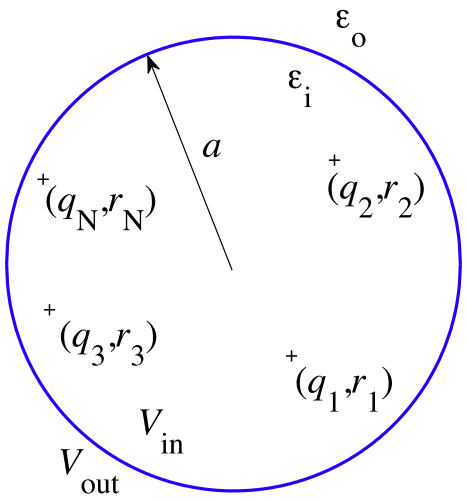

Fig. 2. A spherical dielectric cavity V_{in} of radius a and dielectric permittivity ϵ_i is embedded in the infinite solvent bath V_{out} of dielectric permittivity ϵ_o. A total of N explicit charges of the solute and solvent molecules, say $q_i,\ i = 1, 2, \ldots, N$, are located respectively at $\mathbf{r}_i,\ i = 1, 2, \ldots, N$, inside the spherical cavity.

where the charge distribution $\rho_{\text{in}}(\mathbf{r}) = \sum_{i=1}^{N} q_i \delta(\mathbf{r} - \mathbf{r}_i)$ in which $\delta(\cdot)$ denotes the Dirac delta function, whereas the potential $\Phi_{\text{out}}(\mathbf{r})$ outside the cavity satisfies the following Laplace equation:

$$\Delta\Phi_{\text{out}}(\mathbf{r}) = 0. \tag{2}$$

On the interface Γ between the spherical cavity V_{in} and its surrounding infinite dielectric medium V_{out}, the continuity of the tangential component of the electric field and the normal component of the displacement field requires that

$$\Phi_{\text{out}}|_{\Gamma} = \Phi_{\text{in}}|_{\Gamma} \quad \text{and} \quad \epsilon_{\text{o}} \frac{\partial \Phi_{\text{out}}}{\partial r}\bigg|_{\Gamma} = \epsilon_{\text{i}} \frac{\partial \Phi_{\text{in}}}{\partial r}\bigg|_{\Gamma}. \tag{3}$$

In MD simulations of biomolecules, only the potential $\Phi_{\text{in}}(\mathbf{r})$ inside the cavity V_{in} need be calculated. For simplicity of presentation, here we shall focus our discussion on a single point charge q located at position $\mathbf{r}_{\text{s}}$ inside the spherical cavity V_{in}, as the solution to Eqs. (1)–(3) for multiple point source charges can be obtained using the principle of linear superposition. In this case, the total potential inside the cavity V_{in} can be written as $\Phi_{\text{in}}(\mathbf{r}) = \Phi_{\text{S}}(\mathbf{r}) + \Phi_{\text{RF}}(\mathbf{r})$ where $\Phi_{\text{S}}(\mathbf{r}) = q/(4\pi\epsilon_{\text{i}}|\mathbf{r} - \mathbf{r}_{\text{s}}|)$ is the primary field that results from the source charge and $\Phi_{\text{RF}}(\mathbf{r})$ is the reaction field, respectively. Due to the spherical geometry of the cavity, the reaction field $\Phi_{\text{RF}}(\mathbf{r})$ can be computed analytically by the Kirkwood expansion [15]:

$$\Phi_{\text{RF}}(\mathbf{r}) = \frac{q}{4\pi\epsilon_{\text{i}} a} \sum_{n=0}^{\infty} \frac{(\epsilon_{\text{i}} - \epsilon_{\text{o}})(n+1)}{\epsilon_{\text{i}} n + \epsilon_{\text{o}}(n+1)} \left(\frac{r r_{\text{s}}}{a^2}\right)^n P_n(\cos\theta), \tag{4}$$

where $P_n(\cdot)$ are the Legendre polynomials, and θ is the angle between vectors $\mathbf{r}$ and $\mathbf{r}_{\text{s}}$, respectively.

The Kirkwood series expansion (4) converges quickly for small values of $r/a \ll 1$ and becomes exact at $r = 0$. As a matter of fact, this property has been exploited in some reaction field-based methods of electrostatic interactions [16,17]. On the other hand, when using (4) to calculate the reaction field at a point $\mathbf{r}$ close to the spherical boundary (so $r \approx a$) generated by a source charge located at a point $\mathbf{r}_{\text{s}}$ also close to the spherical boundary (so $r_{\text{s}} \approx a$), the convergence of the Kirkwood series expansion (4) will be very slow due to the fact that $r r_{\text{s}}/a^2 \approx 1$, requiring a large number of terms in the series expansion to achieve high accuracy. And this unpleasant situation will occur in MD simulations since $\Phi_{\text{RF}}(\mathbf{r})$ often has to be computed over the entire cavity [18] in such simulations. As a result, slow convergence is a major limitation of the Kirkwood series expansion in practical computer computations. One way to overcome this problem is the method of images in which the reaction field $\Phi_{\text{RF}}(\mathbf{r})$ at an arbitrary location $\mathbf{r}$ inside the spherical cavity is represented as generated by fictitious point charges located outside the sphere and referred to as image charges.

In fact, it has been found that such a reaction field can be approximated by the potential generated by one single image charge of charge magnitude $q_{\text{k}} = \gamma(a/r_{\text{s}})q$ located outside the sphere at $\mathbf{r}_{\text{k}} = (a/r_{\text{s}})^2 \mathbf{r}_{\text{s}}$, namely,

$$\Phi_{\text{RF}}(\mathbf{r}) \approx \frac{q_{\text{k}}}{4\pi\epsilon_{\text{i}}|\mathbf{r} - \mathbf{r}_{\text{k}}|}, \tag{5}$$

where $\gamma = (\epsilon_{\text{i}} - \epsilon_{\text{o}})/(\epsilon_{\text{i}} + \epsilon_{\text{o}})$ in which ϵ_{i} and ϵ_{o} represents the dielectric permittivity of the spherical dielectric cavity and that of the continuum solvent region outside the spherical cavity, respectively.

Friedman [11] was the first to apply this image approximation of the reaction field in a spherical cavity in the context of biomolecular solvation problems. Due to its simplicity, the Friedman image method has been widely used previously in implicit and hybrid explicit/implicit solvation models [19–24]. The relative approximation error of this simple image method is about $O(\epsilon_{\text{i}}/(\epsilon_{\text{i}} + \epsilon_{\text{o}}))$ [25], so in cases when the solvent medium has a high dielectric constant, such as liquid water, the image approximation of the reaction field given by (5) is sufficiently accurate. For instance, for values of $\epsilon_{\text{i}} = 1$ and $\epsilon_{\text{o}} = 80$ which are typical in biomolecular simulations of aqueous solutions, the error of this approximation could be just in a few percent range. In particular, in the limiting case of $\epsilon_{\text{o}} = \infty$, the analytical representations for the magnitude and the location of the Friedman image reduce to those for the magnitude and the location of the classical Kelvin image [26] for a perfectly conducting sphere in the electrostatic theory, hence the notations.

For better computational accuracy, the ICSM actually employs an image approximation of the reaction field in a spherical cavity using multiple image charges [12]. In short, the same reaction field can be approximated by the potential produced by a set of fictitious charges located along a ray outside the sphere that extends from the Kelvin image location $\mathbf{r}_{\text{k}}$ to infinity, as shown in Fig. 3, namely,

$$\Phi_{\text{RF}}(\mathbf{r}) \approx \frac{q'_{\text{k}}}{4\pi\epsilon_{\text{i}}|\mathbf{r} - \mathbf{r}_{\text{k}}|} + \sum_{m=2}^{N_i} \frac{q'_m}{4\pi\epsilon_{\text{i}}|\mathbf{r} - \mathbf{r}'_m|}, \tag{6}$$

where $q'_{\text{k}} = q_{\text{k}} + q'_1 = (1 + \omega_1\epsilon_{\text{i}}/2\epsilon_{\text{o}})q_{\text{k}}$, and for $m = 2, 3, \ldots, N_i$,

$$q'_m = \frac{\epsilon_{\text{i}}(\epsilon_{\text{i}} - \epsilon_{\text{o}})}{2\epsilon_{\text{o}}(\epsilon_{\text{i}} + \epsilon_{\text{o}})} \frac{\omega_m r_m}{a} q, \quad r_m = r_{\text{k}} \left(\frac{2}{1 - s_m}\right)^{1+\epsilon_{\text{i}}/\epsilon_{\text{o}}}.$$

Here $\{s_m, \omega_m\}_{m=1}^{N_i}$ represent the points and the weights of the Gauss–Radau quadrature [12,27]. Note that when $N_i = 1$, we have $s_1 = -1$ and $\omega_1 = 2$. Therefore, the corresponding single image charge at $\mathbf{r}_{\text{k}}$, termed as the modified Friedman image,

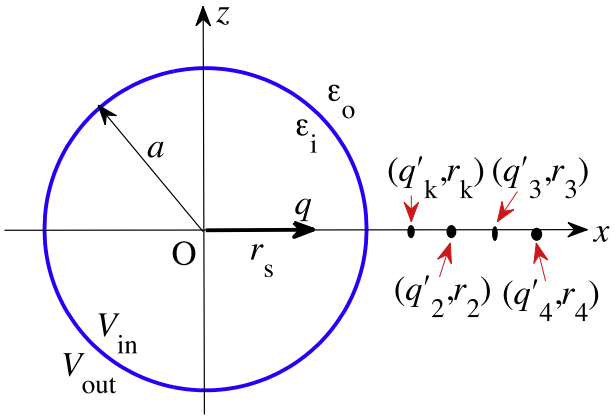

Fig. 3. A schematic illustration of how the reaction field in a spherical cavity V_{in} of radius a and dielectric permittivity ϵ_i is calculated by method of images. The infinite solvent bath V_{out} exterior to the cavity has dielectric permittivity ϵ_o. A point charge q is located on the x-axis at a distance of r_s from the center of the sphere. Then the reaction field inside the cavity generated by this charge can be approximated by the potential created by a set of fictitious charges $q'_k, q'_2, q'_3, \ldots$, referred to as image charges, on the x-axis outside the sphere. The distances from these image charges to the center of the sphere are denoted by $r_k, r_2, r_3, \ldots$, respectively. In particular, the Friedman image method uses only one image charge of magnitude q_k located at $\mathbf{r}_k$.

has a slightly different magnitude $q'_k = (1 + \epsilon_i/\epsilon_o)q_k$ from that of the Friedman image q_k. In general, the greater the number N_i of image charges used, the higher the accuracy of the image approximation of the reaction field.

2.2. Image charge solvation model

In Ref. [9], the image approximation of the reaction field inside a spherical cavity embedded in an infinite solvent bath discussed above was integrated into a hybrid solvation model, leading to the so-called image charge solvation model (ICSM) for electrostatic interactions in computer simulation of biomolecules. Being a hybrid solvation model, as illustrated by Fig. 4, the ICSM contains a central spherical cavity Σ of radius R_c inside which a regular truncated octahedron (TO) simulation box

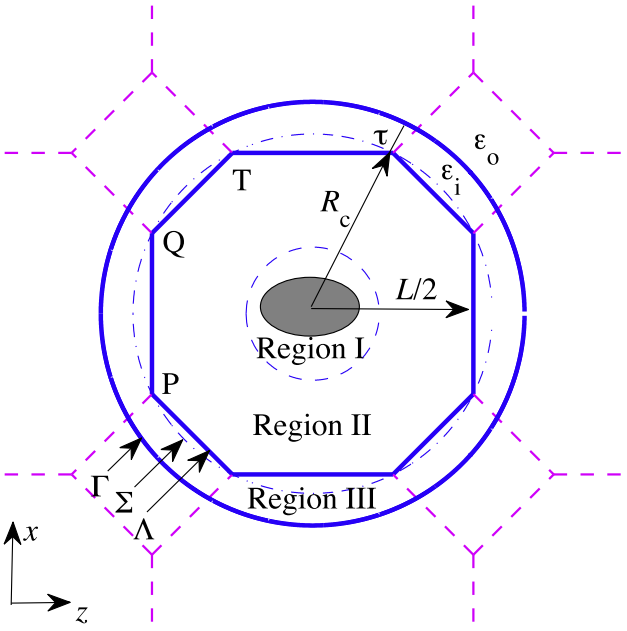

Fig. 4. A schematic representation of the geometry of the ICSM. Shown here is the x–z cross section of the model's geometry if the cubic box, from which the TO simulation box Λ is created, is centered at the origin. The distance from the origin to each of the six square faces of the TO box is $L/2$, to each of the eight hexagonal faces is $\sqrt{3}L/4$, and to each of the 24 corners is $R_c = \sqrt{5}L/4$, respectively. Note that the central octagon in this planar graph is not regular. In fact, each of its four slanted sides such as Side QT represents an edge of the regular TO box and has a length of $\sqrt{2}L/4$, whereas each of its remaining four horizontal or vertical sides such as Side PQ is the diagonal of a square face of the TO box and has a length of $L/2$.

Λ is embedded. Solute and solvent molecules inside Λ are treated explicitly. The regular TO simulation box Λ can be produced by taking a cube and cutting off the eight corners, while preserving the full symmetry of the cube, until exactly one half of the cube's volume is left. In other words, the TO box can be built from a cube of length L by cutting off the eight corners at a distance $\sqrt{2}L/8$ from the center of its faces. For convenience, L is also called the size of such a TO box. The spherical cavity Σ, together with a buffer layer of thickness τ, forms a larger spherical cavity Γ. The solvent molecules outside Λ but inside Γ, marked as "Region III" in Fig. 4, are periodically imaged from the outer part of the simulation box Λ, shown as "Region II" in Fig. 4. The unimaged, inner part of the simulation box, marked as "Region I" in the same figure, forms the productive or useful region of the simulation cell, namely, if the solute under study is placed in Region I, then there will be no periodic images of solute molecules, thus excluding any artificial electrostatic solute–solute interactions. It should be pointed out that a cubic simulation box could also be used in the ICSM but the corresponding productive region would be much smaller in size. Finally, solvent molecules outside the spherical cavity Γ are modeled by a dielectric continuum.

It is noted that, in the hybrid ICSM, only those particles in the main simulation box Λ are real whereas those in Region III are just periodic images of those real particles inside Region II of the simulation box. During the course of the motion in a MD simulation, if a particle leaves the primitive simulation cell Λ on one side, it will then simultaneously enter back into the cell on the other side under the periodic boundary condition (PBC) convention with the same velocity. Also, it is noted that the boundary between Regions I and II is only an imaginary interface inside the simulation cell Λ. If a particle moves into Region II, then it may have periodic images in Region III. Therefore, in order to avoid artificial electrostatic solute–solute interactions, the bio-macromolecule under study need be placed and kept inside Region I during the course of the simulation, which may be achieved by introducing some additional constraints on the bio-macromolecule.

In MD simulations, the trajectories of those real particles inside the main simulation box Λ are to be determined by numerically solving Newton's equations of motion for the system of those interacting particles in Λ, where forces between the particles and potential energy are defined by various molecular mechanic force fields. In particular, in the ICSM, the electrostatic force acting on a particular charge within the main simulation box Λ consists of three parts: its direct Coulomb interaction with all other actual charges inside the simulation box Λ, its direct Coulomb interaction with all periodic images inside Region III including its own periodic images if there are any, and an indirect force conveyed by the reaction field generated from the polarization of the continuum solvent region by all actual and periodic image charges inside the spherical cavity Γ. The two direct Coulomb interactions are calculated basically in a pairwise manner without using any cut-off distance. On the other hand, the electrostatic force derived from the reaction field is approximately computed by methods of images. Other non-bonded, short-range interactions such as the Lennard–Jones interaction are computed using the standard periodic boundary conditions (PBCs) with the minimum-image convention [28].

The ICSM was then applied to study liquid water, and an optimal set of model parameters was obtained that can faithfully represent many structural, dielectric, and dynamic properties of the simulated liquid water [9]. In particular, it was found that the buffer layer should be at least 6 Å in thickness and the single Friedman image is necessary as well as sufficient for the reaction field corrections in actual MD simulations of aqueous solutions. Later in Ref. [10], the ICSM was further tested through simulations of ions solvated in water, and it was shown that the model again can faithfully reproduce known solvation properties of sodium and chloride ions solvated in water. Moreover, in Ref. [29], the ICSM was integrated into the molecular dynamics portion of the TINKER Molecular Modeling package [30], and the integrated package was validated through simulations of liquid water. The results were compared with those obtained by the particle mesh Ewald (PME) method that is built into the TINKER package. Timing performance of the TINKER with the integrated ICSM was benchmarked on bulk water as a function of the size of the simulated system. In particular, timing analysis results showed that the ICSM outperformed the PME for sufficiently large systems with the break-even point at around 30,000 particles in the simulated system.

3. The generalized image charge solvation model

As stated earlier, in general, the greater the number N_i of image charges used, the higher the accuracy of the image approximation of the reaction field in (6). However, it has been demonstrated previously [9,10] that in actual MD simulations of aqueous solution by the ICSM, the results obtained with using one image charge like the Friedman image or the modified Friedman image are accurate enough to reproduce many static and dynamic properties of the simulated water or known solvation properties of the simulated ions solvated in water. In other words, using more than one image charges in the ICSM does not lead to any noticeable difference or improvement in those calculated properties. To the authors, this observation is significant as it suggests the feasibility of using a spheroidal or ellipsoidal cavity in the ICSM. Even though electrostatic image theories for dielectric spheroids or ellipsoids have been found to be far more complicated than those for dielectric spheres, what we really have to do for such kind of applications may be just to develop an accurate enough single-image approximation for the reaction field generated by a single point charge inside such a non-spherical cavity.

3.1. Motivation

In hybrid solvation models, the shape of the central explicit part of the simulated system determines the amount of solvent to be treated explicitly around the solute, and the spherical geometry has often been used because the reaction field in a

dielectric sphere can be solved analytically [15,31]. Moreover, when it need be approximated by methods of images, the image charges of the reaction field are easy to find [11,12,25]. However, this treatment may be inefficient in applications involving non-spherical solutes such as certain globular proteins and other elongated biopolymers like actin and DNA since it will have to include a large number of unnecessary explicit solvent molecules distant from the surface of the solute; see Fig. 5(a). For solutes of irregular shapes, using a non-spherical cavity to incorporate only a few layers of solvent molecules adjacent to the solute would make the size of the simulated system much smaller (see Fig. 5(b)), but how to efficiently obtain an accurate reaction field in a dielectric cavity of such irregular shapes remains a great challenge. In particular, to employ solvation shells with irregular shapes, a Poisson equation need be solved either directly by some numerical methods [32] or by using some approximation theory [7,33] at every simulation time step, which, depending on the system size, may become more computationally intensive than standard explicit all-atom solvent simulations.

Therefore, for studying a bio-macromolecule of irregular shape, it may be more appropriate to adopt a non-spherical but still regular-shaped cavity that can conform closely to the irregular shape of the bio-macromolecule; see Fig. 5(c). While avoiding the use of a spherical cavity reduces the total number of explicit solvent molecules and thus the overall size of the simulated system, employing a regular-shaped cavity (but "less regular" than a sphere) gives us hope that it may be still possible to find some simple but accurate enough image approximations to the reaction field, thus preventing the solution of the Poisson equation at every simulation time step. In the present paper, we particularly aim to extend the hybrid ICSM to use prolate spheroidal or more general triaxial ellipsoidal cavities.

3.2. Electrostatic images of point charges inside a dielectric prolate spheroid

Likely, central to the proposed extension is how to compute the reaction field generated by a single point charge placed inside such a non-spherical cavity by a method of images. While electrostatic image theories for spherical objects, dielectric or perfectly conducting, have been investigated quite extensively in the literature, only a few studies, all being relatively recent, have been dedicated to image theories of spheroidal or ellipsoidal objects. Among those relevant to our purpose/endeavor include the electrostatic image theory for conducting or dielectric prolate spheroids by Lindell et al. [34–38]. Redžić et al. also studied some properties of the image charges for a prolate spheroid [39]. For example, for the perfectly conducting case, it has been found that such an image in general can be represented as a line image charge between the two focal points of the spheroid in terms of Legendre series, or under some special circumstances it can be represented more favorably by a point image charge and a similar but different line image charge along the interfocal line. However, these existing works were mainly limited to the axisymmetric cases in which the external field source is either a point charge on the axis of symmetry or a uniform field. Very recently, Techaumnat et al. presented image charges for a prolate spheroid under an arbitrary external electric field [40]. In order to obtain the equivalent image charges, the so-called cylindrical image charges along the interfocal line of the spheroid need be used, but they are very complicated. Moreover, in all these works the source charge or field is assumed to be external, and to the best of the authors' knowledge, similar electrostatic image theory for source charges inside a prolate spheroidal or ellipsoidal dielectric cavity embedded in a dissimilar dielectric medium has never been published in the literature, probably because there exist some fundamental difficulties for this kind of problems as indicated by some researchers already [35,41].

Therefore, in this work it is not our intention to try to find equivalent image charges for such an electrostatic problem. Rather, we would like to present a simple image approximation and we hope that, when it is integrated into the hybrid ICSM, this simple image approximation becomes accurate enough and the solvation model can thus still be able to faithfully produce the properties of simulated biological systems. To this end and by the principle of superposition of electrostatic fields, theoretically we again shall focus our discussion on a single charge q placed at position $\mathbf{r}_s$ inside a prolate spheroidal cavity of dielectric permittivity ϵ_i embedded in an infinite aqueous solvent of dielectric permittivity ϵ_o, as shown in Fig. 6. Recall that

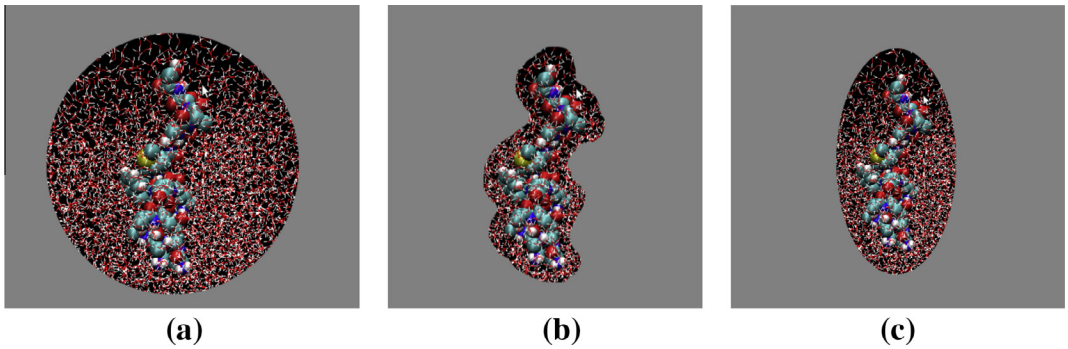

Fig. 5. Hybrid solvation models using cavities of different geometric shapes: (a) a spherical cavity, (b) a cavity that incorporates only a few layers of solvent molecules adjacent to the solute, and (c) a prolate spheroidal or triaxial ellipsoidal cavity. The protein shown here is a Ribonuclease S-peptide.

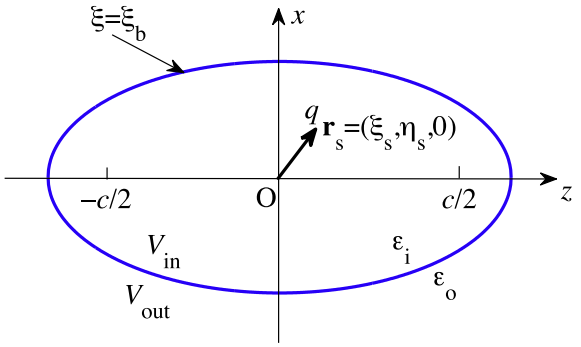

Fig. 6. A point charge q is located at $\mathbf{r}_s = (\xi_s, \eta_s, 0)$ inside a dielectric prolate spheroidal cavity V_{in}. The spheroid is centered at the origin, its polar axis is aligned with the z-axis, and the interfocal distance is c. The spheroidal cavity has dielectric permittivity ϵ_i, while the infinite solvent bath V_{out} exterior to the cavity has dielectric permittivity ϵ_o. In terms of the prolate spheroidal coordinates (ξ, η, ϕ) defined in the main text, the boundary of the prolate spheroidal cavity is given by $\xi = \xi_b$.

the total electrostatic potential inside the cavity, denoted by $\Phi_{in}(\mathbf{r})$, and that outside the cavity, denoted by $\Phi_{out}(\mathbf{r})$, are given by the solutions of the following Poisson and Laplace equations, respectively,

$$\nabla \cdot (\epsilon_i \nabla \Phi_{in}(\mathbf{r})) = -q\delta(\mathbf{r} - \mathbf{r}_s), \tag{7}$$

$$\Delta \Phi_{out}(\mathbf{r}) = 0, \tag{8}$$

coupled with the following interface condition on the interface Γ between the dielectric prolate spheroid and its surrounding dielectric medium:

$$\Phi_{out}|_\Gamma = \Phi_{in}|_\Gamma \quad \text{and} \quad \epsilon_o \frac{\partial \Phi_{out}}{\partial \mathbf{n}}\bigg|_\Gamma = \epsilon_i \frac{\partial \Phi_{in}}{\partial \mathbf{n}}\bigg|_\Gamma, \tag{9}$$

where $\mathbf{n}$ is the outward normal of the interface.

The exact solution to the above electrostatic problem can be found easily and has been well documented in the literature [35,36,42–44]. Assume that the prolate spheroidal cavity is centered at the origin and its polar axis is aligned with the z-axis. Assume further that the prolate spheroid is defined by the equation

$$\frac{x^2 + y^2}{\mathcal{A}^2} + \frac{z^2}{\mathcal{B}^2} = 1, \tag{10}$$

where $\mathcal{B} > \mathcal{A}$. The interfocal distance c is given by $c = 2\sqrt{\mathcal{B}^2 - \mathcal{A}^2}$. Then we adopt the following definition of the prolate spheroidal coordinates (ξ, η, ϕ) defined through

$$x = \frac{c}{2}\sqrt{(\xi^2 - 1)(1 - \eta^2)}\cos\phi, \tag{11a}$$

$$y = \frac{c}{2}\sqrt{(\xi^2 - 1)(1 - \eta^2)}\sin\phi, \tag{11b}$$

$$z = \frac{c}{2}\xi\eta, \tag{11c}$$

where $\xi \in [1, \infty)$ is the radial variable, $\eta \in [-1, 1]$ is the angular variable, and $\phi \in [0, 2\pi]$ is the azimuthal variable, respectively. Note that the surface of constant ξ is a prolate spheroid with interfocal distance c; in particular, $\xi = \xi_b$ with $\xi_b = 2\mathcal{B}/c = \mathcal{B}/\sqrt{\mathcal{B}^2 - \mathcal{A}^2}$ is the prolate spheroid given by (10), and $\xi = 1$ corresponds to the line between the two foci, respectively. Also, the surfaces of constant η are the two sheets of a hyperboloid of revolution with foci $z = \pm c/2$, and the surface of constant ϕ is a plane through the z-axis at an angle ϕ to the x–z plane, respectively.

Without loss of generality, assume that the point charge q is located at the point $\mathbf{r}_s = (x_s, y_s = 0, z_s) = (\xi_s, \eta_s, \phi_s = 0)$ on the x–z plane inside the spheroid defined by the equation $\xi = \xi_b$ (so $1 \leqslant \xi_s < \xi_b$). Then the reaction field Φ_{RF} inside the spheroidal cavity ($1 \leqslant \xi < \xi_b$) is given by the following series expansion [42,43]

$$\Phi_{RF}(\mathbf{r}) = \sum_{n=0}^{\infty}\sum_{m=0}^{n} D_{mn} P_n^m(\xi) P_n^m(\eta)\cos m\phi, \tag{12}$$

where

$$D_{mn} = \frac{q}{4\pi\epsilon_i c} H_{mn} P_n^m(\xi_s) P_n^m(\eta_s) \cdot \frac{(\epsilon_i - \epsilon_o) Q_n^m(\xi_b) Q_n'^m(\xi_b)}{\epsilon_o P_n^m(\xi_b) Q_n'^m(\xi_b) - \epsilon_i Q_n^m(\xi_b) P_n'^m(\xi_b)}. \tag{13}$$

Here, $P_n^m(x)$ and $Q_n^m(x)$ are the associated Legendre functions of the first and the second kind, respectively, and

$$H_{mn} = 2(2n+1)(2-\delta_{m0})(-1)^m\left[\frac{(n-m)!}{(n+m)!}\right]^2,$$

where δ_{m0} is the Kronecker delta.

The semi-analytical series solution given by (12) converges quickly when the field point $\mathbf{r}$ is away from the surface of the spheroid. On the other hand, when calculating the reaction field at a point close to the surface, it converges very slowly, making it inapplicable in practical MD simulations. Recall that in the case of a spherical cavity of radius a, to overcome this limitation, the corresponding reaction field is approximated by the potential generated by a single image charge located outside the sphere, namely, the Friedman image [11]. The magnitude of this image charge is $q_k = \gamma(a/r_s)q$ and the location of the image charge is $\mathbf{r}_k = (a^2/r_s^2)\mathbf{r}_s$ where $\gamma = (\epsilon_i - \epsilon_o)/(\epsilon_i + \epsilon_o)$. Also recall that the location of the classical Kelvin image [26] for a perfectly conducting sphere influenced by an external point charge q located at $\mathbf{r}_s$ is given by the same representation $\mathbf{r}_k = (a^2/r_s^2)\mathbf{r}_s$ and its magnitude is $-(a/r_s)q$, which is exactly the negative of the metallic limit ($\epsilon_i = \infty$) of the magnitude of the Friedman image.

Furthermore, we can recall a more general result [12,45]. Suppose that a sphere of radius a and dielectric permittivity ϵ_i is embedded in a dissimilar infinite dielectric medium of dielectric permittivity ϵ_o. If the source charge q is *outside* the sphere, then for the reaction field *exterior* to the sphere, the position and the magnitude of an image charge are $\mathbf{r}_k = (a^2/r_s^2)\mathbf{r}_s$ and $-\gamma(a/r_s)q$, respectively. On the contrary, if the source charge q is *inside* the sphere, then for the reaction field *interior* to the sphere, the position and the magnitude of an image charge are $\mathbf{r}_k = (a^2/r_s^2)\mathbf{r}_s$ and $\gamma(a/r_s)q$, respectively. As can be seen, for all these cases, the location of the point image is always given by the same formula as that for the classical Kelvin image for a perfectly conducting sphere influenced by an external point charge. On the other hand, the magnitude of the point image is obtained from that of the classical Kelvin image by multiplying the factor γ when the sphere changes from perfectly conducting to dielectric, and/or by changing its sign when the source charge moves from outside to inside the sphere. Based on these observations, we propose that, if we can find an image charge for the reaction field exterior to a perfectly conducting prolate spheroid influenced by an external point charge, then we can obtain an image charge for the reaction field interior to a dielectric prolate spheroid generated by a point charge inside the spheroid in the same manner as how the Friedman image is connected to the classical Kelvin image for a perfectly conducting sphere influenced by an external point charge.

In Appendix, it is shown in detail that the reaction field exterior to a perfectly conducting prolate spheroid influenced by an external point charge q located at $\mathbf{r}_s = (x_s, y_s, z_s) = (\xi_s, \eta_s, \phi_s)$ can be approximated by the potential of a charge of magnitude

$$q_{ind} = -\frac{Q_0(\xi_s)}{Q_0(\xi_b)}q, \tag{14}$$

located at the point $\mathbf{r}_{ind}$ inside the spheroid, where

$$\mathbf{r}_{ind} = \frac{Q_0(\xi_b)}{Q_0(\xi_s)}\left(\frac{Q_1^1(\xi_s)P_1^1(\xi_b)}{Q_1^1(\xi_b)P_1^1(\xi_s)}x_s,\ \frac{Q_1^1(\xi_s)P_1^1(\xi_b)}{Q_1^1(\xi_b)P_1^1(\xi_s)}y_s,\ \frac{Q_1(\xi_s)P_1(\xi_b)}{Q_1(\xi_b)P_1(\xi_s)}z_s\right). \tag{15}$$

The accuracy of this single image approximation depends on the aspect ratio $\mathcal{B}/\mathcal{A}$ of the prolate spheroidal object. In general, the closer the shape of the prolate spheroidal object resembles a sphere, the higher the accuracy of the image approximation. In particular, in the spherical limit ($c \to 0$), namely, when the spheroid approaches a sphere of radius a, the image charge q_{ind} and its location $\mathbf{r}_{ind}$ approach $-(a/r_s)q$ and $\mathbf{r}_k = (a/r_s)^2\mathbf{r}_s$, respectively, where r_s is the distance between the source charge q and the center of the sphere.

Finally, by our earlier argument, we thus propose the following single image approximation for Φ_{RF} as defined in (12), the reaction field interior to a dielectric prolate spheroid generated by a point charge q located at $\mathbf{r}_s = (x_s, y_s, z_s) = (\xi_s, \eta_s, \phi_s)$ inside the spheroid:

$$\Phi_{RF}(\mathbf{r}) \approx \frac{q_p}{4\pi\epsilon_i|\mathbf{r}-\mathbf{r}_{ind}|}, \quad \text{where} \quad q_p = \gamma\frac{Q_0(\xi_s)}{Q_0(\xi_b)}q. \tag{16}$$

Fig. 7 shows a sample distribution of image charges when source charges are uniformly located on the x–z cross section of a prolate spheroid with an aspect ratio of 4/3.

Note that this image approximation has two sources of errors. The first one depends on how close the prolate spheroidal cavity resembles a sphere, and the second one depends on how different the dielectric permittivity of the prolate spheroidal cavity is from that of the surrounding medium. In the spherical limit, the first error vanishes. On the other hand, the second error in relative scale should be in the range of a few percent for typical values of ϵ_i and ϵ_o such as $\epsilon_i = 1$ and $\epsilon_o = 80$, respectively.

3.3. Electrostatic images of point charges inside a dielectric triaxial ellipsoid

The ICSM can be further extended to employ ellipsoidal cavities, which may be desired for simulations of non-spherical or non-spheroidal bio-macromolecules. Similarly, central to this extension is how to approximate the reaction field generated

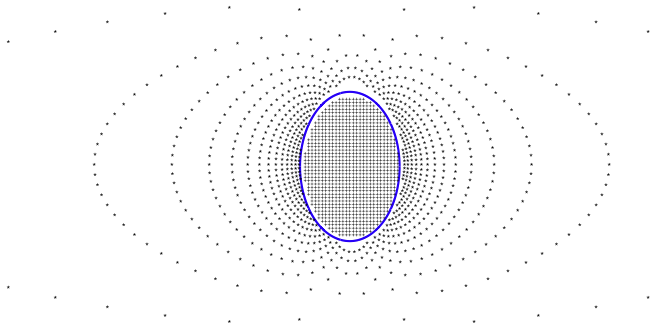

Fig. 7. A sample distribution of image charges when source charges are uniformly located on the x–z cross section of a prolate spheroid with an aspect ratio of 4/3. More precisely, the source charges are located at nodes on a uniform grid.

by a single point charge placed inside a triaxial, namely, scalene, ellipsoidal cavity by image charges. Assume that the triaxial ellipsoidal cavity is defined by the equation

$$\frac{x^2}{A^2}+\frac{y^2}{B^2}+\frac{z^2}{C^2}=1, \tag{17}$$

where $A>B>C>0$ are its semi-axes. Assume further that the Hobson's formalism [46] of the triaxial ellipsoidal coordinates [47–51] is adopted. Then the ellipsoidal coordinates (ξ,μ,ν) corresponding to the point (x,y,z) in the rectangular coordinates, generated by the reference ellipsoid (17), satisfy

$$\frac{x^2}{\lambda^2}+\frac{y^2}{\lambda^2-h^2}+\frac{z^2}{\lambda^2-k^2}=1, \tag{18}$$

where λ stands for either ξ, μ, or ν. The two constants k and h are determined by the semi-focal distances of the reference ellipsoid, namely, $k=\sqrt{A^2-C^2}$ and $h=\sqrt{A^2-B^2}$. Note that every ellipsoidal coordinate has the physical dimension of distance, each one being defined in the intervals $0\leqslant\nu^2\leqslant h^2\leqslant\mu^2\leqslant k^2\leqslant\xi^2<\infty$. The surface of $\xi=$ constant is a triaxial ellipsoid of semi-axes $\xi,\sqrt{\xi^2-h^2}$ and $\sqrt{\xi^2-k^2}$; in particular, $\xi=A$ corresponds to the reference ellipsoid (17), and $\xi=k$ specifies the so-called "fundamental ellipsoid" [41] (also frequently called "the fundamental elliptic disk" [50] or "the focal ellipse" [52])

$$\frac{x^2}{k^2}+\frac{y^2}{k^2-h^2}=1,\quad z=0, \tag{19}$$

respectively. In addition, recall that for the spherical coordinates (r,θ,ϕ), a constant radius r defines a single sphere. Therefore, analogously the variable ξ in the ellipsoidal coordinate system is called radial and assumes only positive values, namely, $\xi\in[k,\infty)$. The transformation between the ellipsoidal and the Cartesian coordinates is [46]

$$x^2=\frac{\xi^2\mu^2\nu^2}{k^2h^2}, \tag{19a}$$

$$y^2=\frac{(\xi^2-h^2)(\mu^2-h^2)(h^2-\nu^2)}{h^2(k^2-h^2)}, \tag{19b}$$

$$z^2=\frac{(\xi^2-k^2)(k^2-\mu^2)(k^2-\nu^2)}{k^2(k^2-h^2)}. \tag{19c}$$

Let us first consider the reaction field exterior to a perfectly conducting and grounded ellipsoidal cavity as illustrated in Fig. 8 that is influenced by an external point charge Q located at $\mathbf{r}_s=(x_s,y_s,z_s)=(\xi_s,\mu_s,\nu_s)$. It is suggested [50] that such reaction field can be approximated first by the potential of a charge of magnitude

$$Q_{\mathrm{ind}}=-\frac{F_0^1(\xi_s)}{F_0^1(\xi_b)}Q \tag{20}$$

located inside the ellipsoid at

$$\mathbf{R}_{\mathrm{ind}}=\frac{F_0^1(\xi_b)}{F_0^1(\xi_s)}\left(\frac{F_1^1(\xi_s)E_1^1(\xi_b)}{F_1^1(\xi_b)E_1^1(\xi_s)}x_s,\ \frac{F_1^2(\xi_s)E_1^2(\xi_b)}{F_1^2(\xi_b)E_1^2(\xi_s)}y_s,\ \frac{F_1^3(\xi_s)E_1^3(\xi_b)}{F_1^3(\xi_b)E_1^3(\xi_s)}z_s\right), \tag{21}$$

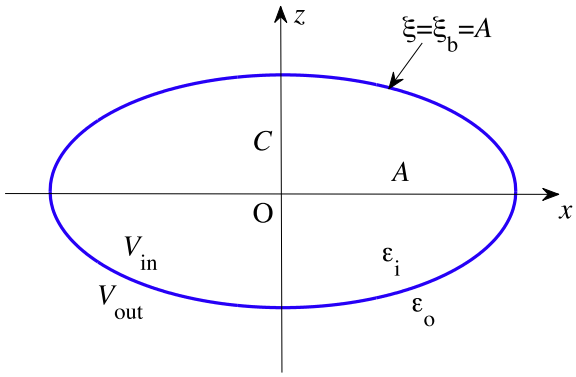

Fig. 8. An ellipsoidal cavity V_{in} of dielectric permittivity ϵ_{i} is embedded in the infinite solvent bath V_{out} of dielectric permittivity ϵ_{o}. The ellipsoid is centered at the origin, and its major principal axis is aligned with the x-axis. In terms of the ellipsoidal coordinates (ξ, μ, ν) defined in the main text, the boundary of the ellipsoidal cavity is given by $\xi = \xi_{\text{b}} = A$. The graph shown represents the x–z cross section of the ellipsoid.

where E_n^p and F_n^p represent the Lamé functions of the first and the second kind of degree n and order p, respectively, in which both indices n and p are positive integers satisfying $2n+1 \geqslant p \geqslant 1$. For the determination of the Lamé functions, see e.g., [53], for a short list of the Lamé functions of the first kind, see e.g., [50], and for numerical computation of the Lamé functions, see e.g., [54–56]. In particular, the lowest Lamé functions of the first kind involved in the image approximation (20) and (21) are given below.

$$E_0^1(\xi) = 1,$$

$$E_1^1(\xi) = \xi,$$

$$E_1^2(\xi) = \sqrt{\xi^2 - h^2},$$

$$E_1^3(\xi) = \sqrt{\xi^2 - k^2}.$$

The corresponding Lamé functions of the second kind can be calculated by [46]

$$F_n^p(\xi) = (2n+1)E_n^p(\xi)\int_{\xi}^{\infty} \frac{\mathrm{d}\xi'}{[E_n^p(\xi')]^2\sqrt{\left(\xi'^2 - h^2\right)\left(\xi'^2 - k^2\right)}}. \tag{22}$$

Now let us consider the reaction field Φ_{RF} interior to a dielectric ellipsoid generated by a point charge q located at $\mathbf{r}_{\text{s}} = (x_{\text{s}}, y_{\text{s}}, z_{\text{s}}) = (\xi_{\text{s}}, \mu_{\text{s}}, \nu_{\text{s}})$ inside the ellipsoid. Semi-analytical series solutions in terms of ellipsoidal harmonics can be easily found [57], but unfortunately, they are too complicated to be used in actual biomolecular dynamics simulations. Therefore, in the same spirit as what we have done for the prolate spheroidal case, we propose the following single image approximation for the reaction field Φ_{RF} inside the ellipsoid

$$\Phi_{\text{RF}}(\mathbf{r}) \approx \frac{q_{\text{e}}}{4\pi\epsilon_{\text{i}}|\mathbf{r} - \mathbf{R}_{\text{ind}}|}, \quad \text{where} \quad q_{\text{e}} = \gamma\frac{F_0^1(\xi_{\text{s}})}{F_0^1(\xi_{\text{b}})}q. \tag{23}$$

Similarly, this image approximation has two sources of errors. One depends on how close the ellipsoidal cavity resembles a sphere. In particular, when the ellipsoid approaches a sphere, q_{e} and $\mathbf{R}_{\text{ind}}$ approach the magnitude and the location of the corresponding Friedman image, respectively. The other one again depends on how different the dielectric permittivity of the ellipsoidal cavity is from that of the surrounding solvent bath.

3.4. The generalized ICSM

For sake of simplifying the discussion, here and in the sequel, we shall focus on the generalized image charge solvation model (GICSM) with using prolate spheroidal cavities. But if really needed, the following discussion can be easily generalized to the case of ellipsoidal cavities. Remember that in the ICSM, a regular truncated octahedron (TO) rather than a cube is used as the main simulation box in order to maximize the size of the productive region. For the same reason, in the GICSM, we use an elongated TO rather than a square prism as the main simulation box. Geometrically, an elongated TO can be obtained by stretching a regular TO in one of the three coordinate directions, say the z direction in this paper. For later convenience, the ratio of its height to its base length, H/L, is called the aspect ratio of the elongated TO and denoted by α. The central octagon shown in Fig. 9 represents the cross section of the elongated TO in the x–z plane if the square prism, from which the

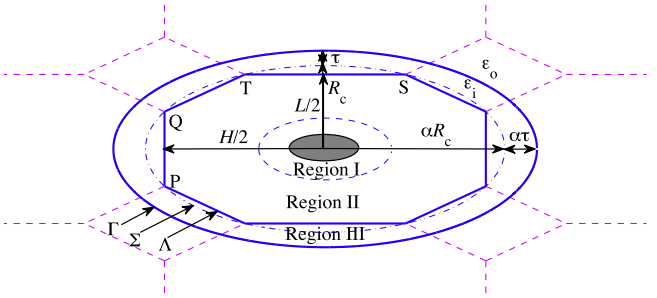

Fig. 9. A schematic representation of the geometry of the GICSM. Shown here is the x–z cross section of the model's geometry if the square prism, from which the elongated TO simulation box Λ is created, is centered at the origin. For the central octagon, each of its four slanted sides such as Side QT represents a longer edge of an elongated hexagonal face and has a length of $\sqrt{L^2+H^2}/4$. Each of the two vertical sides such as Side PQ is the diagonal of a square face and has a length of $L/2$. Each of the two horizontal sides such as Side ST is the longer diagonal of a rhombus face and has a length of $H/2$.

elongated TO is built, is centered at the origin. Note that like a regular TO, an elongated TO remains to be space-filling, a key property that any primitive cell used in computer molecular simulation must possess.

Among the 14 faces of the simulation box, two are identical squares and they are parallel to the x–y plane. Four are identical rhombuses, two of which are parallel to the x–z plane, and the other two parallel to the y–z plane. The remaining eight faces are identical elongated hexagons, two of whose six sides have the same length as that of the square faces and the remaining four have the same length as that of the rhombus faces. Moreover, the equation of the plane containing such an elongated hexagonal face is given by

$$\pm\frac{x}{L}\pm\frac{y}{L}\pm\frac{z}{H}=\frac{3}{4}, \tag{24}$$

imposing + or − depending on which octant the hexagonal face is located in. The distance from the origin to a square face is $H/2$, to a rhombus face $L/2$, and to an elongated hexagonal face $\sqrt{2L^2+H^2}/4$, respectively. On the other hand, the distances from the origin to the 24 corners are not the same any more. The distance to the eight corners on the x–y plane (not shown in Fig. 9) is still given by $R_c=\sqrt{5}L/4$. The distance to the eight corners on the two square faces (such as P and Q in Fig. 9) is given by $R_d=\sqrt{L^2+4H^2}/4$. And the distance to the remaining eight corners (such as S and T in Fig. 9) is given by $R_e=\sqrt{4L^2+H^2}/4$. All these 24 corners are on the surface of the prolate spheroid defined by

$$\frac{x^2}{R_c^2}+\frac{y^2}{R_c^2}+\frac{z^2}{R_f^2}=1,$$

where $R_f=\alpha R_c=\sqrt{5}H/4$, namely,

$$\frac{x^2}{L^2}+\frac{y^2}{L^2}+\frac{z^2}{H^2}=\frac{5}{16}. \tag{25}$$

Now analogously to the ICSM, the generalized ICSM can be briefly described here. As illustrated by Fig. 9, the main elongated TO simulation box Λ is embedded in the central ellipsoidal cavity Σ defined by (25). Solute and solvent molecules inside Λ are treated in atomic detail. The ellipsoidal cavity Σ together with a buffer layer forms a larger ellipsoidal cavity Γ. Then "Region I" (productive region), "Region II", and "Region III" are defined in the same way as how they are defined in the ICSM. The solvent molecules in Region III are periodically imaged from those in Region II, and solvent molecules outside the ellipsoidal cavity Γ are modeled by a dielectric continuum. All other details of the GICSM, being the same as those of the ICSM, can be found in Ref. [9] and thus are omitted here.

Define the thickness of the buffer layer to be the shortest distance between the two ellipsoids Σ and Γ. Note that the two ellipsoids Σ and Γ are closest along their minor axes. Therefore, in order to have a buffer layer of thickness at least τ everywhere between the explicit and the implicit solvents, the semi-minor axis of the ellipsoid Γ must be $R_c+\tau$. For the semi-major axis of the ellipsoid Γ, we can use either $\alpha R_c+\tau$ or $\alpha(R_c+\tau)$. The corresponding ellipsoidal cavity Γ has aspect ratio either smaller than or the same as that of the ellipsoidal cavity Σ. The first choice leads to a buffer layer of relatively uniform thickness, a smaller Region III and thus less computational cost. The second choice, on the other hand, leads to a buffer layer of non-uniform thickness and slightly more computational cost. Also, for the second case, it can be shown that the productive region can accommodate an elongated solute molecule of a maximal minor axis $d_1=(\sqrt{3}-\sqrt{5}/2)L-2\tau$ and a maximal major axis $d_2=\alpha d_1$.

3.5. Key steps of force calculation

In summary, during MD simulations of biomolecules by the GICSM, at each simulation time step, the calculation of the forces acting on all N particles in the main simulation cell Λ involves the following subsequent key steps:

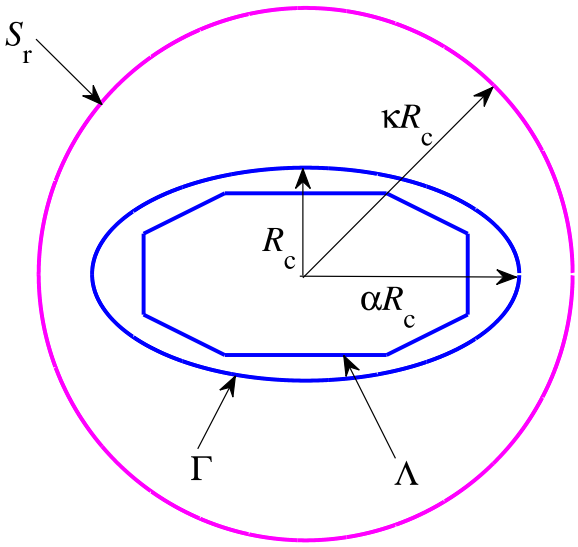

Fig. 10. Schematic illustration of how the FMM together with a separate local expansion procedure is utilized in the GICSM. A reference sphere S_r of radius κR_c is centered at the origin with $\kappa \geqslant \alpha$. The electrostatic force field within the main simulation box Λ due to the sources inside S_r is computed by an adaptive FMM, whereas the electrostatic force field within Λ due to all periodic images and/or image charges of the reaction field outside S_r is calculated by a separate local expansion.

(1) Locate the periodic images of all N actual charges in the unit cell Λ but only keep those inside Region III.
(2) Find the image charges of the reaction field for all charges inside the prolate spheroidal cavity Γ, including all actual charges in the simulation box Λ and all periodic images in Region III.
(3) Evaluate electrostatic interaction forces between all targets (the actual charges in the simulation box Λ) and all sources (actual charges in the simulation box Λ, the periodic images in Region III, and the image charges of the reaction field outside the cavity Γ).
(4) Calculate other short-range, non-electrostatic potential forces such as the Lennard–Jones force using PBCs with the minimum-image convention and cut-off concept.

In the above four steps, each of Steps (1), (2) and (4) requires only $O(N)$ operations. The most time-consuming part is Step (3), namely, calculation of electrostatic forces exerted on all actual charges in the simulation box Λ by all sources. Direct evaluation of such electrostatic forces for all N particles in the unit cell obviously requires $O(N^2)$ operations, but fortunately the fast multipole method (FMM) [13,14,58–61] can be used at this step to reduce the cost from $O(N^2)$ to $O(N)$.

3.6. Order N complexity

As mentioned earlier, one important feature of the ICSM/GICSM lies in the fact that, in practice, it can be easily combined with the FMM, yielding an order N algorithm for computation of electrostatic interactions in biomolecular systems, where N denotes the number of particles in the main simulation cell.

In the simplest implementation, Step (3) can be carried out using one FMM run by including into the FMM level-0 box all actual charges within the unit cell Λ, plus their periodic images in Region III and all image charges of the reaction fields outside the cavity Γ, with all charges being taken as acting in a homogeneous medium of dielectric permittivity ϵ_i. Since the image charges of the reaction field outside the cavity Γ are highly nonuniformly distributed, however, such a direct application of the FMM in the ICSM/GICSM may have to use a big FMM box and thus become inefficient. Luckily, as only the forces for those actual charges in the simulation box Λ need be evaluated, this problem can be efficiently alleviated by a separate local expansion procedure [9]. More specifically, we introduce a reference sphere S_r of radius κR_c centered at the origin with $\kappa \geqslant \alpha$; see Fig. 10. Then the electrostatic force field within the elongated TO box Λ due to the sources inside this reference sphere is evaluated by an adaptive FMM, while that due to the periodic images and/or image charges of the reaction field outside this reference sphere is calculated by the special local expansion procedure whose detail can be found in Ref. [9] and thus is omitted here.

4. Periodic boundary conditions and practical implementation

Periodic boundary conditions (PBCs) are employed in the hybrid ICSM/GICSM in two ways to minimize surface effects [9]. First, they are used to replicate actual particles in the unit cell throughout Region III to form a buffer layer between the

explicit and implicit solvents. Second, they are used to compute other short-range, non-electrostatic interactions just like how these interactions are computed in explicit solvent simulations. For the convenience of potential users of the GICSM, several key implementation details relevant to the PBCs with an elongated TO unit cell are discussed below, where the origin of the coordinate system is assumed to be the center of the elongated TO simulation box.

4.1. Locating periodic images for particles in the unit cell

In the GICSM, actual particles inside the central simulation box Λ are periodically replicated throughout the space between the elongated TO box Λ and the prolate spheroidal cavity Γ. Note that there are 14 nearest neighbors of the central simulation box, each resulting merely from a translation through an appropriate face of the elongated TO. Let (x, y, z) be a point inside the central simulation cell. Then the code to find its periodic image (xi, yi, zi) in each of the 14 surrounding boxes of the central simulation box is fairly easy. Given (24) and the fact that the distance between two opposite hexagonal faces is $\sqrt{2L^2 + H^2}/2$, the FORTRAN code can be written as

```
      m = 0
      DO 1 i = -1, 1
      DO 1 j = -1, 1
      DO 1 k = -1, 1
        IF (ABS(i) + ABS(j) + ABS(k) .NE. 1) GOTO 1
        m = m + 1
        xi(m) = x + i * L
        yi(m) = y  + j * L
        zi(m) = z + k * H
1     CONTINUE
      DO 2 i = -1, 1, 2
      DO 2 j = -1, 1, 2
      DO 2 k = -1, 1, 2
        m = m + 1
        xi(m) = x + i * L/2
        yi(m) = y + j * L/2
        zi(m) = z + k * H/2
2     CONTINUE
```

In fact, the first part of the code is to find the periodic images in six surrounding boxes which share one of the six square or rhombus faces of the central simulation box, while the second part of the code is to find the periodic images in eight surrounding boxes which share one of the eight hexagonal faces of the central simulation box, respectively. It should be recalled that among the 14 periodic images, only those that are located inside the buffer zone are used and thus contribute to the reaction field corrections.

4.2. Bringing particles back into the unit cell

During the course of the MD simulation, only the properties of the unit simulation cell need be recorded and propagated. When a particle leaves the unit simulation cell through one face of the cell, it simultaneously enters back to and reappears in the cell through the opposite face of the cell with the same velocity. This step is also simple to program when using the elongated TO simulation box. Given a particle at an arbitrary location (x, y, z) in the space, the FORTRAN code to bring it back to a location (xi, yi, zi) in the central elongated TO simulation cell is

```
      x = x/L
      y = y/L
      z = z/H
      x = x - ANINT(x)
      y = y - ANINT(y)
      z = z - ANINT(z)
      IF (ABS(x) + ABS(y) + ABS(z) .LT. 0.75) GOTO 1
      x = x - SIGN(0.5, x)
      y = y - SIGN(0.5, y)
      z = z - SIGN(0.5, z)
1     xi = x * L
      yi = y * L
      zi = z * H
```

Note that essentially the first part of the code either brings the particle into the central simulation box or leaves it in one of eight surrounding elongated TO boxes which share one of the eight hexagonal faces of the central simulation box.

4.3. Calculating distance vectors in the minimum-image convention

As in the ICSM [9], other non-bonded, short-range interactions such as the Lennard–Jones interaction are treated by the standard PBCs with the minimum-image convention [28], in which each individual particle in the simulation interacts with the closest image of the remaining particles in the system. The FORTRAN code to calculate the distance vector (dx, dy, dz) between the true nearest-neighbor images of two particles inside the simulation box, say Particle I at (x_i, y_i, z_i) and Particle J at (x_j, y_j, z_j) is

```
      dx = (x(i) − x(j))/L
      dy = (y(i) − y(j))/L
      dz = (z(i) − z(j))/H
      dx = dx − ANINT(dx)
      dy = dy − ANINT(dy)
      dz = dz − ANINT(dz)
      IF (ABS(dx) + ABS(dy) + ABS(dz) .LT. 0.75) GOTO 1
      dx = dx − SIGN(0.5, dx)
      dy = dy − SIGN(0.5, dy)
      dz = dz − SIGN(0.5, dz)
1     dx = dx * L
      dy = dy * L
      dz = dz * H
```

5. Numerical examples

As in Ref. [9], in this section we apply the GICSM to study liquid water [62], and the results are to be analyzed in comparison with those obtained from the ICSM simulations as a reference. As a matter of fact, all MD simulations and trajectory analysis presented here were performed by a program that is modified from the in-house software specifically written for the ICSM project. Therefore, most computational details described in Ref. [9] apply to the present paper. For example, the velocity Verlet algorithm by Jang and Voth [63], coupled with the Nosé–Hoover thermostat, was used for the time integration of the positions and velocities, and in particular, the algorithm labeled VV1 in the original paper was employed. The covalent bond lengths of water molecules were constrained according to the noniterative matrix method [64,65]. The van der Waals interactions were modeled by the Lennard–Jones potential which was truncated at 10 Å. The location of the oxygen atoms was used to measure the distance from one molecule to another. The integration time step was set to 2 fs, the trajectories were recorded every 0.2 ps, and the total simulation time is 1 ns unless otherwise specified. The simulations were performed under constant temperature conditions at $T = 300$ K, and the thermostats coupling constant was 0.05 ps. The dielectric constant of the external field was set to 80.

For FMM implementation, in Ref. [9] the C++ software KIFMM developed by Ying et al. [66] using a kernel-independent adaptive FMM was used. However, in this work we adopt the Fortran software FMM-Yukawa developed by Huang et al. [67,68] using the new version of the adaptive FMM that uses exponential expansions to diagonalize the multipole-to-local translations. The program and its full description are available at http://www.fastmultipole.org/. In all simulations, the maximum number of particles in a leaf, childless box of the adaptive oct-tree structure was set to 80 (*NBOX* = 80). The number of terms in the multipole and local expansion and that in the exponential expansion were both set to 9 for three-digit accuracy (*NTERMS* = 9, *NLAMBS* = 9). For the separate local expansion procedure that is employed to calculate the electrostatic field within the simulation box Λ exerted by the periodic/image charges far away from Λ [9], a sphere of radius $2\alpha(R_c + \tau)$ was employed as the reference sphere, and the local expansion order p in Eq. (13) of Ref. [9] was set to 10.

Unlike in Ref. [9], however, we do not intend to conduct a full-blown numerical analysis of the effect of model parameters, namely, the thickness of the buffer layer and the size of the simulation box. Rather, because it has been demonstrated in Ref. [9] that, in order to obtain a faithful representation of many structural, dielectric, and dynamic properties of the simulated water, a buffer layer of thickness at least 6 Å is required in the ICSM using spherical cavities, the thickness of the buffer layer was set to 6 Å in this work unless otherwise specified. On the other hand, two elongated TO simulation boxes are tested in this work. The first one, named Box A, has $L = 30$ Å and $H = 45$ Å, and the second one, called Box B, has $L = 45$ Å and $H = 60$ Å, respectively. The aspect ratios of these two boxes are 1.5 and 4/3, respectively. Here, these particular numbers of the cell size (30 Å, 45 Å and 60 Å) are chosen simply because they were used in Ref. [9] in testing the ICSM which serves as the reference for the present study. Note that the volume of the regular TO of size L is $L^3/2$ while that of the elongated TO of size $L \times H$ is $L^2H/2$. Therefore, compared to using the corresponding regular TO boxes of size 45 Å and 60 Å, using these two elongated TO simulation boxes can reduce the size of the simulated system by 56% and 44%, respectively. It should also be mentioned that work is on the way to further test the generalized model for cell geometries of larger aspect ratios as well

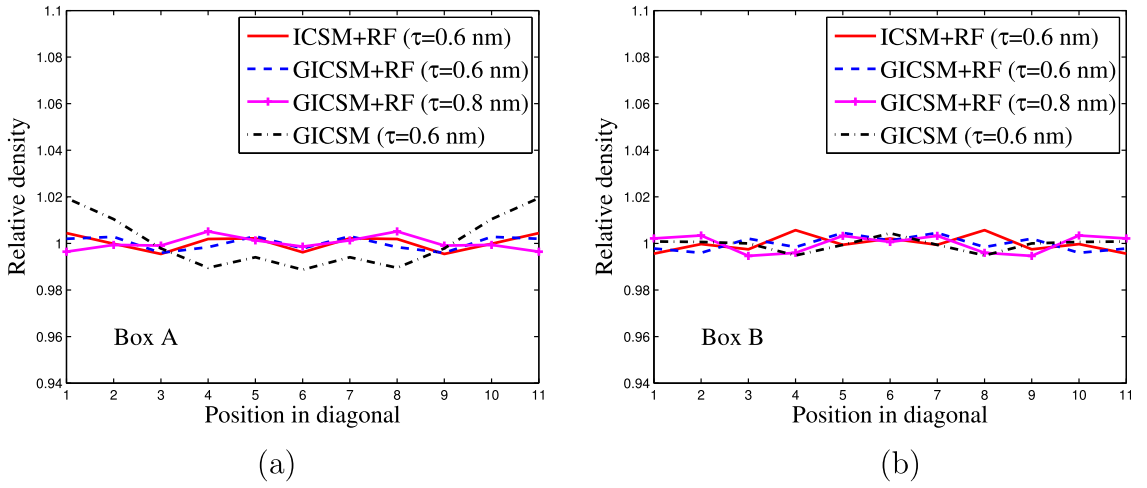

Fig. 11. Relative density along the longer diagonal of the elongated TO boxes with $\tau = 6$ and 8 Å, respectively. Marked here and in the sequel figures/tables, "GICSM" and "GICSM + RF" indicate the GICSM without and with reaction field corrections, respectively. "ICSM + RF" indicates the ICSM with reaction field corrections given by the modified Friedman image charge.

as for other biological systems such as ions solvated in water, and any significant results will be reported in future publications.

5.1. Homogeneity of the simulated liquid water

To validate the GICSM using non-spherical cavities, we investigate several static and dynamic properties of the simulated water and compare the results to those obtained by the ICSM using spherical cavities. First, we investigate whether the generalized model yields the uniform density of the simulated water since the real bulk water is homogeneous. To this end, as in Ref. [9] we examine the local particle density across the simulation box as a measure of the homogeneity of the simulated system. More specifically, we compute the relative density of oxygen atoms along the longer diagonal in the aforementioned two simulation boxes with $\tau = 6$ and 8 Å and the results are displayed in Fig. 11. Also, a summary of density deviations along the diagonal is presented in Table 1. As can be seen, using the GICSM with a buffer layer of at least 6 Å in thickness does yield uniform density of the simulated homogeneous water. Using a thicker buffer layer does not lead to significant improvement in the uniformity of the computed density. In addition, the results seem to indicate that, while reaction field corrections appear to be not critical to yield uniform density as long as the buffer layer of at least 6 Å is used [9], they do improve the results for smaller simulation boxes.

5.2. Oxygen–oxygen radial distribution function of the simulated liquid water

Next, we want to see whether the GICSM can reproduce the structure of the simulated water. To this end, we evaluate the structure using $g_{oo}(r)$, the oxygen–oxygen radial distribution function (RDF) computed over the entire simulation box and the results are displayed in Fig. 12. The most important features of $g_{oo}(r)$ are the locations and magnitudes of the first three density peaks and the first two minima. First and most important of all, the results obtained by the ICSM and by the GICSM for the same simulation box with $\tau = 6$ Å, using or not using reaction field corrections, are almost indistinguishable. Second, as it has been demonstrated already in Ref. [9], our work also show that the effect of the reaction field to the RDF is small and is almost negligible when the thickness of the buffer layer is 6 Å, indicating that the presence of the reaction field is not critical for the proper description of the static structure. Note that the structure of water is not very sensitive to the reaction field corrections has been noted previously [69]. As far as the RDF's dependence on the geometric parameters of the simulation box, recall that when using the ICSM with spherical cavities, it has been shown that such structural property is not strongly affected by the size L of the simulation box as well as the thickness τ of the buffer layer. More precisely, on the one hand,

Table 1
Standard deviations of relative densities along the longer diagonal of elongated TO boxes.

	ICSM + RF		GICSM + RF		GICSM	
	$\tau = 6$ Å	$\tau = 8$ Å	$\tau = 6$ Å	$\tau = 8$ Å	$\tau = 6$ Å	$\tau = 8$ Å
Box A	0.003	0.003	0.003	0.003	0.011	0.009
Box B	0.003	0.002	0.003	0.004	0.003	0.016

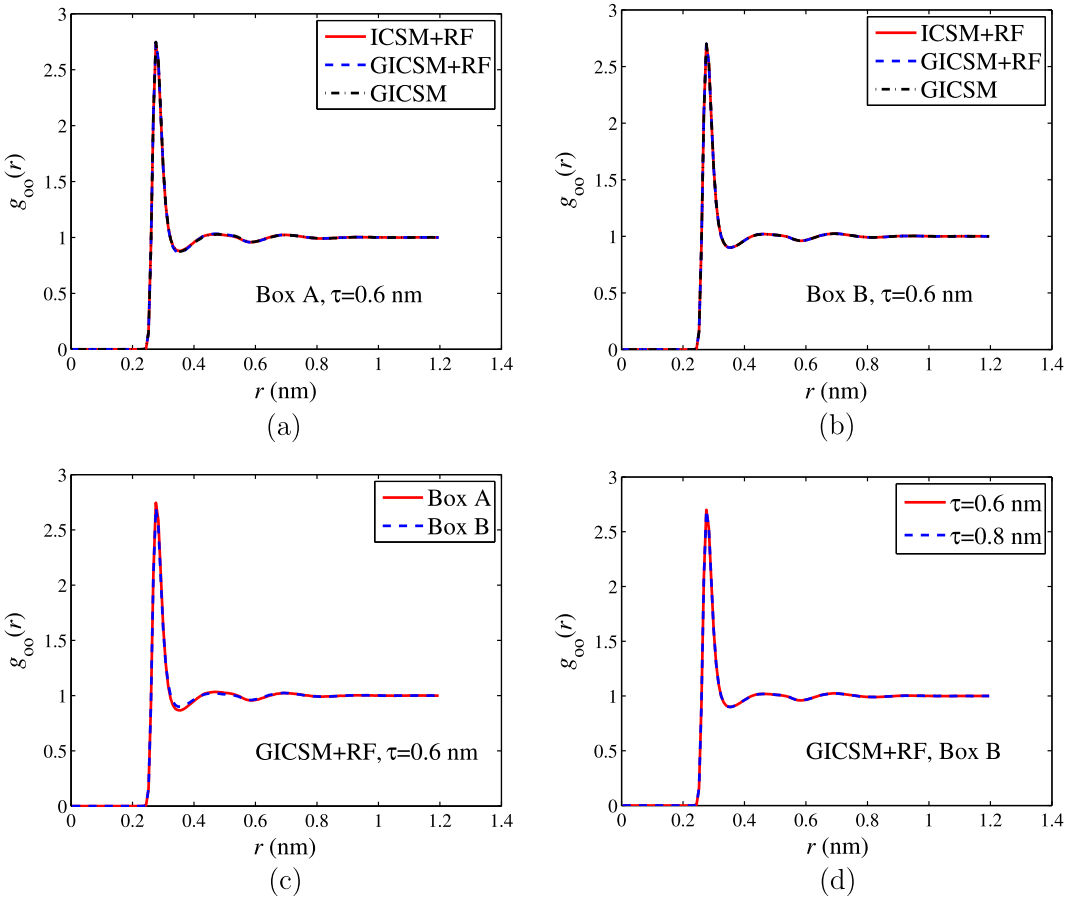

Fig. 12. Oxygen–oxygen RDFs computed in this work. (a)–(c) RDFs obtained by the ICSM and the GICSM, using or not using reaction field corrections, for different simulation boxes with $\tau = 6$ Å. (d) Comparison between RDFs obtained by the GICSM using reaction field corrections for Box B with $\tau = 6$ and 8 Å, respectively.

regarding the RDF's dependence on the thickness τ of the buffer layer, it has been shown that increasing τ leads to convergence for all sizes of the simulation box considered there, and in particular, the changes in the RDFs become almost unnoticeable for $\tau \geqslant 4$ Å. The conclusion was that, in order to reproduce the structure of liquid water correctly, the thickness of the buffer layer need be at least 4 Å. As shown in Fig. 12(d), RDFs obtained by the GICSM using reaction field corrections for Box B with $\tau = 6$ and 8 Å, respectively, are indeed almost unnoticeable. On the other hand, regarding the RDF's dependence on the size of the simulation box, the results presented here also confirm the previous finding by the ICSM that the RDFs are more sensitive to the size of the simulation box than to the thickness of the buffer layer. For example, Fig. 12(c) compares RDFs obtained by the GICSM using reaction field corrections for both Box A and Box B with $\tau = 6$ Å, respectively. As can be seen, there are noticeable variations in $g_{oo}(r)$ although only the magnitudes of the first two density peaks and the first minimum are slightly different. A closer look at data reveals that the first peaks lie at 2.8 Å; the magnitude is 2.75 for Box A and 2.70 for Box B, respectively. For the first density minimum, the position is around 3.6 Å and the magnitude is 0.87 for Box A and 0.90 for Box B, respectively. The second peaks lie at around 4.7 Å; the magnitude is 1.03 for Box A and 1.02 for Box B, respectively. Importantly, the RDFs computed for Box B are in excellent agreement with those results obtained in the particle mesh Ewald (PME) [70] calculations that were reported in Ref. [9].

5.3. Self-diffusion coefficient of the simulated liquid water

Finally, we test whether the GICSM can still give us the proper description of diffusion of the simulated water. To this end, we choose to evaluate the self-diffusion coefficient D, a transport coefficient characterizing how quickly equilibrium is established in particle density following a small perturbation. Here the diffusion coefficient is calculated by least squares fitting a straight line ($y = Dt$). The results of these studies are summarized in Table 2.

Recall that when using the ICSM with spherical cavities, it has been shown that the thickness of the buffer layer τ has no noticeable effect on D except for the smallest simulation box $L = 30$ Å. For larger systems, $L = 45$ and 60 Å, the diffusion coef-

Table 2
Diffusion coefficients D with error estimates (unit of $D: 10^{-9}$ m^2s^{-1}).

	ICSM + RF		GICSM + RF		GICSM	
	$\tau = 6$ Å	$\tau = 8$ Å	$\tau = 6$ Å	$\tau = 8$ Å	$\tau = 6$ Å	$\tau = 8$ Å
Box A	6.26 ± 0.01	6.25 ± 0.01	6.28 ± 0.01	6.26 ± 0.01	9.63 ± 0.17	16.87 ± 0.58
Box B	6.08 ± 0.01	6.11 ± 0.01	6.08 ± 0.01	6.07 ± 0.01	6.92 ± 0.03	7.99 ± 0.08

ficient remains within a statistical error for varying τ. Also, like the structural function, the diffusion coefficient strongly depends on the size of the simulation box. Generally speaking, small simulation boxes overestimate the mobility of water molecules, and increasing the simulation box size can progressively improve the diffusion constant with the convergence typically seen at $L = 60$ Å for the ICSM. The same conclusion can be drawn from the results obtained by the GICSM with reaction field corrections. For example, the diffusion coefficient changes from 6.28×10^{-9} m^2 s^{-1} for $\tau = 6$ Å to only 6.26×10^{-9} m^2 s^{-1} for $\tau = 8$ Å if using Box A, and from 6.08×10^{-9} m^2 s^{-1} to only 6.07×10^{-9} m^2 s^{-1} if using Box B, respectively, reaffirming that the dependence of the diffusion on the thickness of the buffer layer is not strong especially when larger simulation boxes are utilized. But on the contrary, when using the same thickness for the buffer layer, the diffusion coefficient drops from 6.28×10^{-9} m^2 s^{-1} for Box A to 6.08×10^{-9} m^2 s^{-1} for Box B if $\tau = 6$ Å, and from 6.26×10^{-9} m^2 s^{-1} to 6.07×10^{-9} m^2 s^{-1} if $\tau = 8$ Å.

Most importantly, however, it has been shown in Ref. [9] that reaction field correction is essential for the proper description of the diffusion and on the other hand, using only the reaction field correction from the Friedman image charge or the modified Friedman image charge is enough for the ICSM to achieve such a proper description of the diffusion. Again, the same conclusion can be drawn from the results presented in the present paper. First, it clearly shows that, without reaction field correction, the GICSM substantially overestimates the mobility of water molecules, for both simulation boxes as well as both thicknesses of the buffer layer considered. Second, although the single image charge approximation proposed in the present paper for the reaction field inside a dielectric prolate spheroidal cavity is very raw, the corresponding reaction field correction seems to be still sufficient for the GICSM to reproduce the dynamic diffusion of the simulated water properly. Note that for either box or either thickness of the buffer layer, the results obtained by the ICSM using only the modified Friedman image charge correction and the GICSM using the proposed single image charge correction agree each other within a statistical error. In summary, we come to the same conclusion that reaction field correction and sufficiently large simulation box are required to properly describe self-diffusion processes.

6. Conclusions

We extended in this paper the hybrid image charge solvation model (ICSM) using spherical cavities to prolate spheroidal and triaxial ellipsoidal cavities in order to more efficiently simulate bio-macromolecules of non-spherical shapes. The generalized model, termed as the generalized image charge solvation model (GICSM), was validated using liquid water as a test system, and the results were analyzed and compared with those obtained from the ICSM simulations. We found that the results obtained by the generalized model were in excellent agreement with those obtained by the ICSM using corresponding larger spherical cavities, indicating its potential to become an accurate but more efficient alternative to the ICSM when bio-macromolecules of irregular shapes are to be simulated.

In addition to the utilization of a general truncated octahedron as the MD simulation box, central to the GICSM is an image approximation method to compute the reaction field for a point charge placed inside a prolate spheroidal or triaxial ellipsoidal cavity by using a single image charge located outside the cavity. The results presented in this paper showed that, although the single image charge approximation is very raw, the corresponding reaction field correction seems to be still sufficient for the GICSM to reproduce the dynamic diffusion property of the simulated water. Therefore, it is the authors' belief that the single image approximation presented in this paper for the GICSM could be used in other reaction field-based solvation models too.

Generally speaking, the GICSM shares the same advantages and disadvantages as the ICSM. Over lattice-sum explicit solvent methods such as the Ewald method and the particle mesh Ewald (PME) method, a major advantage of the ICSM/GICSM lies in the fact that they are designed for inhomogeneous systems and they are free of periodic artifacts in electrostatic interactions. Therefore, they can be applied in areas where the PME is not suitable, including tests on the effects of periodicity artifacts, simulations of highly charged solutes, and pKa determinations of proteins. On the other hand, while the ICSM/GICSM has a better asymptotic computational complexity $O(N)$ than the $O(N \log N)$ complexity of the PME, when used to simulate homogeneous systems of relatively small sizes, the PME was found significantly more efficient. However, in a separate project [29], we also found that, when integrated into TINKER [30], the ICSM becomes computationally more efficient than the PME built into TINKER when 30,000 or more explicit atoms are included in the simulated system.

Finally, it should be admitted that for the GICSM to be used as a general tool, it needs to be further investigated, not only by considering simulation cells of larger aspect ratios to see how far the physical properties of the liquid water can hold up as the aspect ratio is changed, but also by testing it through simulations of other biological systems such as ions solvated in water and systems that contain peptides to see whether known properties of these systems can also be faithfully reproduced

by the generalized model. Systematic study in both directions is in progress, and significant findings will be reported in future publications.

Acknowledgments

The support of the National Institutes of Health through Grant No. 1R01GM083600-04 is gratefully acknowledged. C. Xue thanks the support of the National Natural Science Foundation of China (Grant No. 10971181) for the work reported in this paper. S. Deng was also supported by funds provided by the University of North Carolina at Charlotte.

Appendix A. Conducting prolate ellipsoid influenced by a point charge

Let us consider a perfectly conducting prolate spheroid centered at the origin and embedded in a homogeneous medium of dielectric permittivity ϵ_o. The interfocal distance of the spheroid is assumed to be c; see Fig. 6. Without loss of generality, let a point charge q be located at the point $\mathbf{r}_s = (\xi_s, \eta_s, \phi_s{=}0)$ in the x–z plane outside the spheroid defined by the equation $\xi = \xi_b$ (so $\xi_s > \xi_b \geqslant 1$). The electric potential outside the spheroid can be expressed as

$$\Phi_{out}(\mathbf{r}) = \frac{q}{4\pi\epsilon_o|\mathbf{r}-\mathbf{r}_s|} + \sum_{n=0}^{\infty}\sum_{m=0}^{n} A_{mn} Q_n^m(\xi) P_n^m(\eta)\cos m\phi, \tag{26}$$

where A_{mn} are the undetermined expansion coefficients. Moreover, note that the general expansion of $1/|\mathbf{r}-\mathbf{r}_s|$ in the prolate spheroidal coordinates is given by [46,53,71]

$$\frac{1}{|\mathbf{r}-\mathbf{r}_s|} = \frac{1}{c}\sum_{n=0}^{\infty}\sum_{m=0}^{n} H_{mn} P_n^m(\eta_s) P_n^m(\eta)\cos m\phi \begin{cases} P_n^m(\xi_s) Q_n^m(\xi), & \xi > \xi_s, \\ P_n^m(\xi) Q_n^m(\xi_s), & \xi < \xi_s. \end{cases}$$

Therefore, the electric potential in the range $\xi_b \leqslant \xi \leqslant \xi_s$ can be alternatively expressed as

$$\Phi_{out}(\mathbf{r}) = \sum_{n=0}^{\infty}\sum_{m=0}^{n}\left[A_{mn} Q_n^m(\xi) + \frac{q}{4\pi\epsilon_o c} H_{mn} Q_n^m(\xi_s) P_n^m(\eta_s) P_n^m(\xi)\right] P_n^m(\eta)\cos m\phi. \tag{27}$$

Furthermore, when the spheroid is conducting and grounded, it can be found

$$A_{mn} = -q\frac{H_{mn} Q_n^m(\xi_s) P_n^m(\eta_s) P_n^m(\xi_b)}{4\pi\epsilon_o c Q_n^m(\xi_b)} \tag{28}$$

by requiring that $\Phi(\mathbf{r}) = 0$ at the surface of the spheroid $\xi = \xi_b$.

Recall that in the spherical limit ($c \to 0$), one has $(c/2)\xi \to r$, where r stands for the radial variable of the spherical coordinates. Also note that as $\xi \to \infty$, $Q_0^0(\xi) \to 1/\xi$. Therefore, for large ξ, the $n = 0$ term is proportional to r^{-1} and thus corresponds to the total charge induced on the spheroid:

$$q_{ind} = -q\frac{Q_0(\xi_s)}{Q_0(\xi_b)}. \tag{29}$$

The same result could also be found by integrating the charge density

$$\rho_{ind}(\eta,\phi) = -\epsilon_o \mathbf{n}\cdot(\nabla\Phi_{out})|_{\xi=\xi_b} = -\epsilon_o\left(\frac{1}{h_\xi}\frac{\partial\Phi_{out}}{\partial\xi}\right)\Big|_{\xi=\xi_b} \tag{30}$$

over the surface of the spheroid, namely,

$$q_{ind} = \int_0^{2\pi}\int_{-1}^{1} \rho_{ind}(\eta,\phi) h_\eta h_\phi \,\mathrm{d}\eta\,\mathrm{d}\phi, \tag{31}$$

where h_ξ, h_η, and h_ϕ are the scale factors for the prolate spheroidal coordinates (ξ,η,ϕ)

$$h_\xi = \frac{c}{2}\sqrt{\frac{\xi^2-\eta^2}{\xi^2-1}},$$

$$h_\eta = \frac{c}{2}\sqrt{\frac{\xi^2-\eta^2}{1-\eta^2}},$$

$$h_\phi = \frac{c}{2}\sqrt{(\xi^2-1)(1-\eta^2)}.$$

In fact, substituting (30) into (31) yields

$$q_{\text{ind}} = \frac{q}{8\pi}\sum_{n=0}^{\infty}\sum_{m=0}^{n} H_{mn} Q_n^m(\xi_{\text{s}}) P_n^m(\eta_{\text{s}})(\xi_{\text{b}}^2 - 1)\frac{W_n^m(\xi_{\text{b}})}{Q_n^m(\xi_{\text{b}})}\int_0^{2\pi}\int_{-1}^{1} P_n^m(\eta)\cos m\phi \,\mathrm{d}\eta\,\mathrm{d}\phi, \tag{32}$$

where $W_n^m(x)$ represents the Wronskian relation between $P_n^m(x)$ and $Q_n^m(x)$ given by

$$W_n^m(x) = P_n^m(x)Q_n^{m\prime}(x) - P_n^{m\prime}(x)Q_n^m(x) = \frac{N_{\text{s}}}{1-x^2}\frac{(n+m)!}{(n-m)!},$$

with $N_{\text{s}} = 1$ for $|x| < 1$ and $N_{\text{s}} = (-1)^m$ otherwise. So we have

$$q_{\text{ind}} = \frac{q}{8\pi}\sum_{n=0}^{\infty}\sum_{m=0}^{n}\mathcal{H}_{mn}(\xi_{\text{s}},\xi_{\text{b}})\int_0^{2\pi}\int_{-1}^{1} P_n^m(\eta)\cos m\phi \,\mathrm{d}\eta\,\mathrm{d}\phi, \tag{33}$$

where

$$\mathcal{H}_{mn}(\xi_{\text{s}},\xi_{\text{b}}) = (-1)^{m+1}H_{mn}\frac{Q_n^m(\xi_{\text{s}})P_n^m(\eta_{\text{s}})}{Q_n^m(\xi_{\text{b}})}\frac{(n+m)!}{(n-m)!}.$$

By the orthogonality of $\cos m\phi$ and that of $P_n^m(\cdots)$, we get

$$\int_0^{2\pi}\int_{-1}^{1} P_n^m(\eta)\cos m\phi \,\mathrm{d}\eta\mathrm{d}\phi = \begin{cases} 4\pi, & \text{if } m = n = 0,\\ 0, & \text{otherwise.}\end{cases}$$

And note that $H_{00} = 2$, and $P_0^0(x) \equiv P_0(x) \equiv 1$, we finally have

$$q_{\text{ind}} = -q\frac{Q_0(\xi_{\text{s}})}{Q_0(\xi_{\text{b}})}.$$

The centroid $\mathbf{r}_{\text{ind}} = (x_{\text{ind}}, y_{\text{ind}}, z_{\text{ind}})$ of the induced charge distribution, which undoubtedly is located inside the prolate spheroid, is obtained as

$$\mathbf{r}_{\text{ind}} = \frac{1}{q_{\text{ind}}}\int_0^{2\pi}\int_{-1}^{1}\mathbf{r}\rho_{\text{ind}}(\eta,\phi)h_\eta h_\phi \,\mathrm{d}\eta\,\mathrm{d}\phi, \tag{34}$$

namely,

$$\mathbf{r}_{\text{ind}} = -\frac{Q_0(\xi_{\text{b}})}{8\pi Q_0(\xi_{\text{s}})}\sum_{n=0}^{\infty}\sum_{m=0}^{n}\mathcal{H}_{mn}(\xi_{\text{s}},\xi_{\text{b}})\int_0^{2\pi}\int_{-1}^{1}\mathbf{r}P_n^m(\eta)\cos m\phi \,\mathrm{d}\eta\,\mathrm{d}\phi. \tag{35}$$

First, note that $z = (c/2)\xi_{\text{b}}\eta$ on the surface of the spheroid. So we have

$$\int_0^{2\pi}\int_{-1}^{1} zP_n^m(\eta)\cos m\phi \,\mathrm{d}\eta\,\mathrm{d}\phi = \frac{c}{2}\xi_{\text{b}}\int_0^{2\pi}\int_{-1}^{1}\eta P_n^m(\eta)\cos m\phi \,\mathrm{d}\eta\,\mathrm{d}\phi.$$

Again, by the orthogonality of $\cos m\phi$ and that of $P_n^m(\cdots)$ (note $\eta = P_1^0(\eta)$), we get

$$\int_0^{2\pi}\int_{-1}^{1}\eta P_n^m(\eta)\cos m\phi \,\mathrm{d}\eta\,\mathrm{d}\phi = \begin{cases}\frac{4\pi}{3}, & \text{if } m = 0,\ n = 1,\\ 0, & \text{otherwise.}\end{cases}$$

Consequently, we obtain

$$z_{\text{ind}} = \frac{Q_0(\xi_{\text{b}})}{Q_0(\xi_{\text{s}})}\cdot\frac{Q_1(\xi_{\text{s}})P_1(\eta_{\text{s}})}{Q_1(\xi_{\text{b}})}\cdot\frac{c}{2}\xi_{\text{b}}, \tag{36}$$

which, by noting that $P_1(x) = x$, can be rewritten as

$$z_{\text{ind}} = \frac{Q_0(\xi_{\text{b}})}{Q_0(\xi_{\text{s}})}\cdot\frac{Q_1(\xi_{\text{s}})P_1(\xi_{\text{b}})}{Q_1(\xi_{\text{b}})P_1(\xi_{\text{s}})}\cdot\left(\frac{c}{2}\xi_{\text{s}}\eta_{\text{s}}\right). \tag{37}$$

Then finally, by invoking (11c), we have

$$z_{\text{ind}} = \frac{Q_0(\xi_{\text{b}})}{Q_0(\xi_{\text{s}})}\cdot\frac{Q_1(\xi_{\text{s}})P_1(\xi_{\text{b}})}{Q_1(\xi_{\text{b}})P_1(\xi_{\text{s}})}\cdot z_{\text{s}}. \tag{38}$$

Now let us consider the x coordinate of the centroid. By (11a), we have

$$\int_0^{2\pi}\int_{-1}^{1} xP_n^m(\eta)\cos m\phi \,\mathrm{d}\eta\,\mathrm{d}\phi = \frac{c}{2}\sqrt{\xi_{\text{b}}^2 - 1}\int_0^{2\pi}\int_{-1}^{1}\sqrt{1-\eta^2}\cos\phi P_n^m(\eta)\cos m\phi \,\mathrm{d}\eta\,\mathrm{d}\phi.$$

Recall that

$$P_1^1(x) = \begin{cases} \sqrt{x^2-1}, & |x| \geqslant 1, \\ -\sqrt{1-x^2}, & |x| < 1. \end{cases} \tag{39}$$

Therefore, we get

$$\int_0^{2\pi}\int_{-1}^{1} \sqrt{1-\eta^2}\cos\phi P_n^m(\eta)\cos m\phi \,\mathrm{d}\eta\,\mathrm{d}\phi = \begin{cases} -\frac{4\pi}{3}, & \text{if } m=n=1, \\ 0, & \text{otherwise.} \end{cases}$$

Consequently, we have

$$x_{\mathrm{ind}} = \frac{Q_0(\xi_{\mathrm{b}})}{Q_0(\xi_{\mathrm{s}})}\cdot\frac{Q_1^1(\xi_{\mathrm{s}})P_1^1(\eta_{\mathrm{s}})}{Q_1^1(\xi_{\mathrm{b}})}\cdot\left(-\frac{c}{2}\sqrt{\xi_{\mathrm{b}}^2-1}\right), \tag{40}$$

which, by noting (39) and that $\phi_{\mathrm{s}} = 0$, can be rewritten as

$$x_{\mathrm{ind}} = \frac{Q_0(\xi_{\mathrm{b}})}{Q_0(\xi_{\mathrm{s}})}\cdot\frac{Q_1^1(\xi_{\mathrm{s}})P_1^1(\xi_{\mathrm{b}})}{Q_1^1(\xi_{\mathrm{b}})P_1^1(\xi_{\mathrm{s}})}\cdot\left(\frac{c}{2}\sqrt{\xi_{\mathrm{s}}^2-1}\sqrt{1-\eta_{\mathrm{s}}^2}\cos\phi_{\mathrm{s}}\right). \tag{41}$$

Then finally, by invoking (11a), we have

$$x_{\mathrm{ind}} = \frac{Q_0(\xi_{\mathrm{b}})}{Q_0(\xi_{\mathrm{s}})}\cdot\frac{Q_1^1(\xi_{\mathrm{s}})P_1^1(\xi_{\mathrm{b}})}{Q_1^1(\xi_{\mathrm{b}})P_1^1(\xi_{\mathrm{s}})}\cdot x_{\mathrm{s}}. \tag{42}$$

Finally, by using the fact that for any integer m,

$$\int_0^{2\pi}\sin\phi\cos m\phi\,\mathrm{d}\phi = 0,$$

we immediately obtain $y_{\mathrm{ind}} = 0$ for the case that $\mathbf{r}_{\mathrm{s}} = (x_{\mathrm{s}}, y_{\mathrm{s}}{=}0, z_{\mathrm{s}}) = (\xi_{\mathrm{s}}, \eta_{\mathrm{s}}, \phi_{\mathrm{s}}{=}0)$, namely, when the source charge is on the x–z plane, so is the centroid of the induced charge distribution. For the general case that $\mathbf{r}_{\mathrm{s}} = (x_{\mathrm{s}}, y_{\mathrm{s}}, z_{\mathrm{s}})$, by the underlying symmetry of the x and the y coordinates in our setting, we immediately have

$$y_{\mathrm{ind}} = \frac{Q_0(\xi_{\mathrm{b}})}{Q_0(\xi_{\mathrm{s}})}\cdot\frac{Q_1^1(\xi_{\mathrm{s}})P_1^1(\xi_{\mathrm{b}})}{Q_1^1(\xi_{\mathrm{b}})P_1^1(\xi_{\mathrm{s}})}\cdot y_{\mathrm{s}}.$$

So in conclusion, the centroid of the charge distribution induced on the surface of a conducting prolate spheroid influenced by an external point charge q located at $\mathbf{r}_{\mathrm{s}} = (x_{\mathrm{s}}, y_{\mathrm{s}}, z_{\mathrm{s}})$ is given by

$$\mathbf{r}_{\mathrm{ind}} = \frac{Q_0(\xi_{\mathrm{b}})}{Q_0(\xi_{\mathrm{s}})}\left(\frac{Q_1^1(\xi_{\mathrm{s}})P_1^1(\xi_{\mathrm{b}})}{Q_1^1(\xi_{\mathrm{b}})P_1^1(\xi_{\mathrm{s}})}x_{\mathrm{s}},\ \frac{Q_1^1(\xi_{\mathrm{s}})P_1^1(\xi_{\mathrm{b}})}{Q_1^1(\xi_{\mathrm{b}})P_1^1(\xi_{\mathrm{s}})}y_{\mathrm{s}},\ \frac{Q_1(\xi_{\mathrm{s}})P_1(\xi_{\mathrm{b}})}{Q_1(\xi_{\mathrm{b}})P_1(\xi_{\mathrm{s}})}z_{\mathrm{s}}\right). \tag{43}$$

The significance of the centroid of the induced charge distribution lies in the fact that it gives us the first approximation for the location of the induced charge. In other words, we can approximate the reaction field exterior to the spheroid by the potential of an image charge of magnitude q_{ind} located at $\mathbf{r}_{\mathrm{ind}}$. Assume that a point charge of magnitude q_{ind} is placed at $\mathbf{r}_{\mathrm{ind}}$. Then we write the reaction field as

$$\Phi_{\mathrm{RF}}(\mathbf{r}) = \frac{q_{\mathrm{ind}}}{4\pi\epsilon_{\mathrm{o}}|\mathbf{r}-\mathbf{r}_{\mathrm{ind}}|} + \sum_{n=0}^{\infty}\sum_{m=0}^{n} A'_{mn}Q_n^m(\xi)P_n^m(\eta)\cos m\phi, \tag{44}$$

where

$$A'_{mn} = A_{mn} - \frac{q_{\mathrm{ind}}}{4\pi\epsilon_{\mathrm{o}}c}H_{mn}P_n^m(\xi_{\mathrm{ind}})P_n^m(\eta_{\mathrm{ind}}) = -\frac{q}{4\pi\epsilon_{\mathrm{o}}c}H_{mn}\left[\frac{Q_n^m(\xi_{\mathrm{s}})P_n^m(\eta_{\mathrm{s}})P_n^m(\xi_{\mathrm{b}})}{Q_n^m(\xi_{\mathrm{b}})} - \frac{Q_0(\xi_{\mathrm{s}})}{Q_0(\xi_{\mathrm{b}})}P_n^m(\xi_{\mathrm{ind}})P_n^m(\eta_{\mathrm{ind}})\right]. \tag{45}$$

Note that obviously $A'_{00} = 0$, namely, the residual series represents the potential due to a neutral charge distribution. Moreover, as a consequence of the location of the image charge q_{ind} at the center of charge of the prolate spheroid, the coefficients for $n = 1$ (namely, the dipole terms) in the residual series are also zero, namely, $A'_{01} = A'_{11} = 0$. Indeed, note that $z_{\mathrm{s}} = (c/2)\xi_{\mathrm{s}}\eta_{\mathrm{s}} = (c/2)P_1(\xi_{\mathrm{s}})P_1(\eta_{\mathrm{s}})$ and

$$P_1(\xi_{\mathrm{ind}})P_1(\eta_{\mathrm{ind}}) = \xi_{\mathrm{ind}}\eta_{\mathrm{ind}} = \frac{2z_{\mathrm{ind}}}{c} = \frac{Q_0(\xi_{\mathrm{b}})}{Q_0(\xi_{\mathrm{s}})}\cdot\frac{Q_1(\xi_{\mathrm{s}})P_1(\xi_{\mathrm{b}})P_1(\eta_{\mathrm{s}})}{Q_1(\xi_{\mathrm{b}})}.$$

Then it is easy to see that $A'_{01} = 0$. On the other hand, note that $\phi_{\mathrm{ind}} = 0$ when $\mathbf{r}_{\mathrm{s}} = (\xi_{\mathrm{s}}, \eta_{\mathrm{s}}, \phi_{\mathrm{s}} = 0)$. We have

$$P_1^1(\xi_{\mathrm{ind}})P_1^1(\eta_{\mathrm{ind}}) = -\sqrt{\xi_{\mathrm{ind}}^2-1}\sqrt{1-\eta_{\mathrm{ind}}^2}\cos\phi_{\mathrm{ind}} = -\frac{2x_{\mathrm{ind}}}{c},$$

which, by plugging x_{ind} given by (42), can be written as

$$P_1^1(\xi_{\text{ind}})P_1^1(\eta_{\text{ind}}) = \frac{Q_0(\xi_b)}{Q_0(\xi_s)} \frac{Q_1^1(\xi_s)P_1^1(\xi_b)P_1^1(\eta_s)}{Q_1^1(\xi_b)}.$$

Then it is also easy to see that $A'_{11} = 0$. Therefore, we actually have

$$\Phi_{\text{RF}}(\mathbf{r}) = \frac{q_{\text{ind}}}{4\pi\epsilon_o|\mathbf{r} - \mathbf{r}_{\text{ind}}|} + \sum_{n=2}^{\infty}\sum_{m=0}^{n} A'_{mn} Q_n^m(\xi) P_n^m(\eta)\cos m\phi. \tag{46}$$

The closer the shape of the prolate spheroidal body resembles a sphere, the faster the modified coefficients A'_{mn} in the residual series for $n \geqslant 2$ converge. In particular, in the spherical limit ($c \to 0$), A'_{mn} approaches zero for all n and m, while the induced charge and its center approach $-(a/r_s)q$ and $\mathbf{r}_k = (a/r_s)^2\mathbf{r}_s$, respectively, where a is the radius of the limiting sphere and r_s the distance of the source charge and the center of the sphere.

References

[1] P. Koehl, Electrostatics calculations: latest methodological advances, Curr. Opin. Struct. Biol. 16 (2006) 142–151.
[2] R.M. Levy, E. Gallicchio, Computer simulations with explicit solvent: recent progress in the thermodynamic decomposition of free energies and in modeling electrostatic effects, Annu. Rev. Phys. Chem. 49 (1998) 531–567.
[3] C. Sagui, T.A. Darden, Molecular dynamics simulation of biomolecules: long-range electrostatic effects, Annu. Rev. Biophys. Biomol. Struct. 28 (1999) 155–179.
[4] M. Feig, C.L. Brooks III, Recent advances in the development and application of implicit solvent models in biomolecule simulations, Curr. Opin. Struct. Biol. 14 (2004) 217–224.
[5] N.A. Baker, Improving implicit solvent simulations: a Poisson-centric view, Curr. Opin. Struct. Biol. 15 (2005) 137–143.
[6] A. Okur, C. Simmerling, Hybrid explicit/implicit solvation methods, in: D.C. Spellmeyer (Ed.), Annual Reports in Computational Chemistry, vol. 2, Elsevier, Amsterdam, 2006, pp. 97–109 (Ch. 6).
[7] M.S. Lee, F.R. Salsbury Jr., M.A. Olson, An efficient hybrid explicit/implicit solvent method for biomolecular simulations, J. Comput. Chem. 25 (2004) 1967–1978.
[8] M.S. Lee, M.A. Olson, Evaluation of Poisson solvation models using a hybrid explicit/implicit solvent method, J. Phys. Chem. B 109 (2005) 5223–5236.
[9] Y. Lin, A. Baumketner, S. Deng, Z. Xu, D. Jacobs, W. Cai, An image-based reaction field method for electrostatic interactions in molecular dynamics simulations of aqueous solutions, J. Chem. Phys. 131 (2009) 154103.
[10] Y. Lin, A. Baumketner, S. Song, S. Deng, D. Jacobs, W. Cai, Ionic solvation studied by image-charge reaction field method, J. Chem. Phys. 134 (2011) 044105.
[11] H.L. Friedman, Image approximation to the reaction field, Mol. Phys. 29 (1975) 1533–1543.
[12] W. Cai, S. Deng, D. Jacobs, Extending the fast multipole method to charges inside or outside a dielectric sphere, J. Comput. Phys. 223 (2007) 846–864.
[13] L. Greengard, The Rapid Evaluation of Potential Fields in Particle Systems, MIT Press, Cambridge, MA, 1987.
[14] L. Greengard, V. Rokhlin, A fast algorithm for particle simulations, J. Comput. Phys. 73 (1987) 325–348.
[15] J.G. Kirkwood, Theory of solutions of molecules containing widely separated charges with special applications to zwitterions, J. Chem. Phys. 2 (1934) 351–361.
[16] J.A. Barker, R.O. Watts, Monte-Carlo studies of dielectric properties of water-like models, Mol. Phys. 26 (1973) 789–792.
[17] I.G. Tironi, R. Sperb, P.E. Smith, W.F. van Gunsteren, A generalized reaction field method for molecular dynamics simulation, J. Chem. Phys. 102 (1995) 5451–5459.
[18] H. Alper, R.M. Levy, Dielectric and thermodynamic response of a generalized reaction field model for liquid state simulations, J. Chem. Phys. 99 (1993) 9847–9852.
[19] J.A.C. Rullmann, P.T.V. Duijnen, Analysis of discrete and continuum dielectric models; application to the calculation of protonation energies in solution, Mol. Phys. 61 (1987) 293–311.
[20] A. Wallqvist, On the implementation of Friedman boundary conditions in liquid water simulations, Mol. Simul. 10 (1993) 13–17.
[21] R. Abagyan, M. Totrov, Biased probability Monte Carlo conformational searches and electrostatic calculations for peptides and proteins, J. Mol. Biol. 235 (1994) 983–1002.
[22] L. Wang, J. Hermans, Reaction field molecular dynamics simulation with Friedman's image charge method, J. Phys. Chem. 99 (1995) 12001–12007.
[23] J.J. Havranek, P.B. Harbury, Tanford–Kirkwood electrostatics for protein modeling, Proc. Natl. Acad. Sci. USA 96 (1999) 11145–11150.
[24] G. Petraglio, M. Ceccarelli, M. Parrinello, Nonperiodic boundary conditions for solvated systems, J. Chem. Phys. 123 (2005) 044103.
[25] S. Deng, W. Cai, D. Jacobs, A comparable study of image approximations to the reaction field, Comput. Phys. Commun. 177 (2007) 689–699.
[26] J.D. Jackson, Classical Electrodynamics, John Wiley, New York, 1999.
[27] W. Gautschi, Algorithm 726; ORTHPOL – a package of routines for generating orthogonal polynomials and Gauss-type quadrature rules, ACM T. Math. Softw. 20 (1994) 21–62.
[28] M.P. Allen, D.J. Tildesley, Computer Simulation of Liquids, Oxford University Press, Oxford, 1987.
[29] K. Baker, A. Baumketner, Y. Lin, S. Deng, D. Jacobs, W. Cai, An order *N* method for calculating the electrostatic potential added to TINKER, Comput. Phys. Commun. 184 (2013) 19–26.
[30] J.W. Ponder, TINKER – software tools for molecular design, 2004, <http://dasher.wustl.edu/ffe/downloads/guide.pdf>.
[31] J.G. Kirkwood, Statistical mechanics of liquid solutions, Chem. Rev. 19 (1936) 275–307.
[32] W. Im, S. Bernèche, B. Roux, Generalized solvent boundary potential for computer simulations, J. Chem. Phys. 114 (2001) 2924–2937.
[33] D. Bashford, D.A. Case, Generalized Born models of macromolecular solvation effects, Annu. Rev. Phys. Chem. 51 (2000) 129–152.
[34] J.C.-E. Sten, I.V. Lindell, An electrostatic image theory for the conducting prolate spheroid, J. Electromagn. Waves Appl. 9 (1995) 599–604.
[35] I.V. Lindell, K.I. Nikoskinen, Electrostatic image theory for the dielectric prolate spheroid, J. Electromagn. Waves Appl. 15 (2001) 1075–1096.
[36] I.V. Lindell, G. Dassios, K.I. Nikoskinen, Electrostatic image theory for the conducting prolate spheroid, J. Phys. D: Appl. Phys. 34 (2001) 2302–2307.
[37] D.V. Redžić, Comment on electrostatic image theory for the dielectric prolate spheroid by I.V. Lindell and K.I. Nikoskinen, J. Electromagn. Waves Appl. 17 (2003) 1625–1627.
[38] I.V. Lindell, K.I. Nikoskinen, Electrostatic image theory for the dielectric prolate spheroid, reply to comments by D. Redzic, J. Electromagn. Waves Appl. 17 (2003) 1627–1628.
[39] D.V. Redžić, S.S. Redžić, Image charge inclusions in the prolate dielectric spheroid, J. Phys. D: Appl. Phys. 38 (2005) 3991–3994.
[40] B. Techaumnat, M. Washizu, Equivalent image charges of a prolate spheroid under an external electric field, J. Electrostat. 69 (2011) 388–393.
[41] T. Miloh, The ultimate image singularities for external ellipsoidal harmonics, SIAM J. Appl. Math. 26 (1974) 334–344.
[42] D.V. Redžić, An electrostatic problem: a point charge outside a prolate dielectric spheroid, Am. J. Phys. 62 (1994) 1118–1121.
[43] S. Deng, Electrostatic potential of point charges inside dielectric prolate spheroids, J. Electrostat. 66 (2008) 549–560.
[44] S. Deng, Electrostatic potential of point charges inside dielectric oblate spheroids, J. Electrostat. 67 (2009) 807–814.
[45] W.T. Norris, Charge images in a dielectric sphere, IEE Proc. – Sci. Meas. Technol. 142 (1995) 142–150.

[46] E.W. Hobson, The Theory of Spherical And Ellipsoidal Harmonics, Cambridge University Press, Cambridge, England, 1931.
[47] T. Miloh, Forces and moments on a tri-axial ellipsoid in potential flow, Israel J. Technol. 11 (1973) 63–74.
[48] J.W. Perram, P.J. Stiles, On the application of ellipsoidal harmonics to potential problems in molecular electrostatics and magnetostatics, Proc. R. Soc. Lond. A 349 (1976) 125–139.
[49] T. Miloh, Maneuvering hydrodynamics of ellipsoidal forms, J. Ship Res. 23 (1979) 66–75.
[50] J.C.-E. Sten, Ellipsoidal harmonics and their application in electrostatics, J. Electrostat. 64 (2006) 647–654.
[51] L.C. Lew Yan Voon, M. Willatzen, On triaxial ellipsoidal quantum dots, J. Phys. Condens. Matter 16 (2004) 1087–1093.
[52] G. Dassios, F. Kariotou, Magnetoencephaloggraphy in ellipsoidal geometry, J. Math. Phys. 44 (2003) 220–241.
[53] P.M. Morse, H. Feshbach, Methods of Theoretical Physics, McGraw-Hill, New York, 1953.
[54] R. Garmier, J.-P. Barriot, Ellipsoidal harmonic expansions of the gravitational potential: Theory and application, Celest. Mech. Dyn. Astron. 79 (2000) 235–275.
[55] S. Ritter, On the computation of lamé functions, of eigenvalues and eigenfunctions of some potential operators, ZAMMZ. Angew. Math. Mech. 78 (1998) 66–72.
[56] H.-J. Dobner, S. Ritter, Verified computation of lamé functions with high accuracy, Computing 60 (1998) 81–89.
[57] C. Xue, S. Deng, Three-layer dielectric models for generalized Coulomb potential calculation in ellipsoidal geometry, Phys. Rev. E 83 (2011) 056709.
[58] L. Greengard, V. Roklin, A new version of the fast multipole method for the Laplace equation in three dimensions, Acta Numer. 6 (1997) 229–269.
[59] H. Cheng, L. Greengard, V. Roklin, A fast adaptive multipole algorithm in three dimensions, J. Comput. Phys. 155 (1999) 468–498.
[60] L. Greengard, J. Huang, A new version of the fast multipole method for screened Coulomb interactions in three dimensions, J. Comput. Phys. 180 (2002) 642–658.
[61] B. Lu, X. Cheng, J. Huang, J.A. McCammon, Order *N* algorithm for computation of electrostatic interactions in biomolecular systems, Proc. Natl. Acad. Sci. USA 103 (2006) 19314–19319.
[62] W.L. Jorgensen, J. Chandrasekhar, J.D. Madura, R.W. Impey, M.L. Klein, Comparison of simple potential functions for simulating liquid water, J. Chem. Phys. 79 (1983) 926–935.
[63] S. Jang, G.A. Voth, Simple reversible molecular dynamics algorithms for Nosé–Hoover chain dynamics, J. Chem. Phys. 107 (1997) 9514–9526.
[64] G. King, A. Warshel, A surface constrained all-atom solvent model for effective simulations of polar solutions, J. Chem. Phys. 91 (1989) 3647–3660.
[65] P.K. Yang, S.H. Liaw, C. Lim, Representing an infinite solvent system with a rectangular finite system using image charges, J. Phys. Chem. B 106 (2002) 2973–2982.
[66] L. Ying, G. Biros, D. Zorin, A kernel-independent adaptive fast multipole method in two and three dimensions, J. Comput. Phys. 196 (2004) 591–626.
[67] J. Huang, J. Jia, B. Zhang, FMM-Yukawa: an adaptive fast multipole method for screened Coulomb interactions, Comput. Phys. Commun. 180 (2009) 2331–2338.
[68] B. Zhang, J. Huang, N.P. Pitsianis, X. Sun, Revision of FMM-Yukawa: an adaptive fast multipole method for screened Coulomb interactions, Comput. Phys. Commun. 181 (2010) 2206–2207.
[69] P.H. Hunenberger, W.F. van Gunsteren, Alternative schemes for the inclusion of a reaction-field correction into molecular dynamics simulations: Influence on the simulated energetic, structural, and dielectric properties of liquid water, J. Chem. Phys. 108 (1998) 6117–6134.
[70] U. Essmann, L. Perera, M.L. Berkowitz, T. Darden, H. Lee, L. Pedersen, A smooth particle mesh Ewald method, J. Chem. Phys. 103 (1995) 8577–8593.
[71] W.R. Smythe, Static and Dynamic Electricity, third ed., Hemisphere, New York, 1989.